DIGITAL HOLOGRAPHIC DIAGNOSTICS OF AERATED-LIQUID JETS IN A SUBSONIC CROSSFLOW

By

BRIAN DERRICK MILLER

Bachelor of Science Mechanical Engineering

Oklahoma Christian University

Oklahoma City, Oklahoma

2004

Submitted to the Faculty of the
Graduate College of the
Oklahoma State University
in partial fulfillment of
the requirements for
the Degree of
MASTER OF SCIENCE
December, 2006

DIGITAL HOLOGRAPHIC DIAGNOSTICS OF

AERATED-LIQUID JETS IN A SUBSONIC

CROSSFLOW

Thesis Approved:

Khaled A. Sallam

Dr. Khaled A. Sallam, Thesis Advisor

Andrew S. Arena

Dr. Andrew S. Arena, Committee Member

Frank W. Chambers

Dr. Frank W. Chambers, Committee Member

A. Gordon Emslie

A. Gordon Emslie, Dean of the Graduate College

Acknowledgements

I wish to express my appreciation for my wife and all of her support, understanding, and love. She has been a great help throughout this research. I am also thankful for all of the support, assistance, guidance, and friendship from my advisor, Dr. Khaled A. Sallam. I also express my gratitude to Dr. Andrew S. Arena Jr. and Dr. Frank W. Chambers for their advice and participation on the thesis committee. Finally, I would like to thank Dr. Kuo-Cheng Lin and Dr. Mohammed Bingabr for all of their assistance.

This research was sponsored by Taitech, Inc., under a subcontract from Taitech's base contract with the U.S. Air Force. Initial development of experimental methods was carried out under the sponsorship of Oklahoma NSF EPSCoR (NanoNet). Support from the NASA Oklahoma Space Grant fellowship is also gratefully acknowledged.

Table of Contents

List of Figures

List of Tables

Nomenclature

Alphabetical

a	= experimental coefficient used in calculation of discharge coefficient
A^*	= discharge orifice area
A_a	= total area of air injection holes
ALR	= aerating gas-to-liquid mass flow rate ratio
b	= experimental coefficient used in calculation of discharge coefficient
C_d	= discharge coefficient
C_{dw}	= discharge coefficient for water
D^*	= discharge orifice diameter
d_{max}	= maximum drop diameter for each test condition
d_l	= ligament diameter
d_L	= film thickness
d_0	= injector orifice diameter
GLR	= aerating gas-to-liquid mass flow rate ratio
h	= spray plume penetration height
h_0	= non-aerated spray plume penetration height
L	= length of injector mixing chamber
M	= Mach number
m	= mass flow rate
MMD	= mass median diameter

N = number of pixels

p_c = mixing chamber pressure

Q = volumetric flow rate

$Q_{L,\ injected}$ = volumetric flow rate of liquid injected

$Q_{G,\ injected}$ = volumetric flow rate of gas injected

q = jet/freestream momentum flux ratio, $\rho_L v_j^{\ 2} / \rho_\infty u_\infty^{\ 2}$

q_0 = non-aerated jet/freestream momentum flux ratio

u = velocity component in the crossflow direction

v = velocity component in jet streamwise direction

V_{rel} = droplet speed relative to gas phase

$V_{rel,x}$ = droplet speed relative to gas phase in the x direction

$V_{rel,y}$ = droplet speed relative to gas phase in the y direction

w = width of spray plume

SMD = Sauter mean diameter, $\sum d_i^{\ 3} / \sum d_i^{\ 2}$, i for all droplets

X = dummy variable used in calculation of discharge coefficient

x = cross-stream distance

y = streamwise distance

z = downstream distance

Greek

α = converging angle after the mixing chamber

β = flow-average void fraction

λ = wavelength of light

μ = dynamic viscosity

ν = kinematic viscosity

ρ = density

σ = surface tension

$\Delta\xi$ = smallest distance resolved

Subscripts

0 = property at GLR = 0

a = aeration property

G = aerating gas property

j = jet exit property

L = liquid property

l = ligament property

w = water property

∞ = ambient gas property

Abstract

The properties of aerated liquid jets in gaseous crossflow have been studied by many. It has been proven to produce a dense spray of fine droplets. Its properties have been studied downstream in the less dense far-field region as well as directly at the injector exit. However, the dense near-field region has proven to be optically challenging for techniques such as Phase Doppler Particle Anemometry (PDPA). There are many non-spherical droplets packed closely together which cause these techniques to be ineffective.

To measure the properties of the droplets in this region different holographic techniques were investigated to determine their effectiveness. Digital holographic techniques were chosen over traditional film-based techniques to avoid the expensive, time consuming, and hazardous film development process. In-line techniques were chosen over off-axis techniques which are usually used with the film based methods because it kept the resolution requirements low for the lower resolution digital sensors.

Two digital holographic methods in particular were examined. The first was standard digital in-line holography (DIH), and the second was digital holographic microscopy (DHM). Digital in-line holography worked well for resolving large structures but was limited in its ability to resolve the small details in the spray. Digital holographic microscopy was then investigated because of its ability to resolve very small details. It proved to be the best method of the two, providing valuable information about the small droplets encountered in the spray. Both techniques are also insensitive to the non-spherical droplets encountered in this region.

Using DHM the spray structure was studied in this near injector area. Droplet sizes and distributions were recorded for a 3-D volume (50 mm x 105 mm x 25 mm) of spray at downstream locations of 25 and 50 jet diameters. At these locations the effects of jet diameter, gas-to-liquid mass flow rate ratio (GLR), and jet-to-freestream momentum ratio were observed. It was found that the GLR has the most effect on drop size distribution. Increasing the GLR caused the drop sizes to decrease. It was also found that jet diameter had little effect on the droplet sizes, which can be explained based on the thickness of the liquid film inside the injector. The effect of jet-to-freestream momentum ratio increased the penetration height of the spray into the crossflow. All of these effects were observed through three dimensional plots of the Sauter mean diameter (SMD), volume fraction plots, and drop size distributions.

Chapter 1.

Introduction

1.1 Background

The ability to produce small droplets is of interest in many industries and is especially important to combustion applications, where smaller drop sizes mean more surface area for the reaction to take place. Many different techniques have been developed to produce these sprays containing small droplets. The simplest way to do this is to decrease the injector exit diameter which will decrease droplet sizes. This causes many problems because very high injection pressures are needed to achieve reasonable flow rates and very small exit diameters are prone to clogging.

To overcome these problems other methods have been devised that mix a gas phase with the liquid being injected known as "twin fluid injection." The gas phase serves to add energy to the liquid phase which assists in breaking up the liquid. One of these methods is known as air blast injection which uses large volumes of air at a low velocity to help break up the fluid. Another method is flash atomization which raises the temperature of the liquid above its boiling point or dissolves a gas in the liquid which creates bubbles that expand in the liquid causing it to break.

These methods work well but it is not always convenient to raise a liquid to its boiling point or to dissolve gas into the liquid phase, and air blast injection is not as

effective as the other methods. Another "twin fluid" method is aerated injection (also known as effervescent atomization). It is characterized by a two phase flow consisting of a liquid and a gas. This two phase flow occurs inside the injector where the gas and liquid are injected in a way so that they are mixed before they leave the injector exit. This is similar to the flash atomization because it produces gas bubbles which assist in atomization without the complications of dissolving gas or heating the liquid to its boiling point.

1.2 Problem Statement

There is a lack of information about the properties of the spray produced by aerated-liquid injectors in a gaseous crossflow. Its properties have been studied far downstream where the spray is less dense, and its properties have been studied at the injector exit. However, there is a lack of information between these two regions because of the dense spray of often non-spherical droplets which proves to be inaccessible to other optical techniques such as Phase Doppler Particle Anemometry (PDPA). The objectives of the present investigation were to use different digital holographic diagnostics to complete experimental measurements of the spray structure produced by aerated liquid jet in gaseous crossflow in the dense spray near-injector region in order to fill this gap of information.

1.3 Previous Studies

1.3.1 Aerated Liquid Injectors

The properties of aerated injection have been studied by many because of its ability to produce a fine spray of small droplets. Previous results have revealed much about aerated injection and how the different input parameters affect the type of spray that is produced. Some of these input parameters are injector geometry, the ratio of gas to liquid mass flow rate (GLR), injection pressure, viscosity of the injected liquid, and the jet-to-freestream momentum ratio to name a few. Studies were first done by Lefebvre et al. [1] introducing the injector and focusing mainly on the effects of injector pressure and injector exit diameters.

In addition to experimental work some theoretical work has been done describing what is happening inside the injector. Each different setup consists of some way to inject the gas and the liquid phases together so that they will mix inside the injector. Most designs fall into two basic categories [2], outside-in or inside-out injection.

With outside-in injection, the liquid is injected by some type of tube in the center of the injector and the gas is introduced by small holes on the outer wall of the injector. Inside-out injection has just the opposite setup, the inner tube is perforated and is responsible for delivering the gas while the liquid flows around the outer edge (see Figure 1-1). It is suggested that the inside out setup performs better for low liquid flow rates while the outside in setup performs better for high liquid flow rates [2]. There is no real evidence to support this claim and is simply a suggestion by the author, since there have been no studies directly comparing the two different setups.

The most important dimensions used in aerated injectors is the length to diameter ratio of the final discharge orifice and the converging angle downstream of the mixing chamber [3]. These dimensions are used to determine the coefficient of discharge, C_d, of the injector which describes the pressure needed for a certain mass flow rate. In aerated injectors this value is calculated for water, C_{dw}, by Eqs. 1.1 and 1.2:

$$C_{D_W} = aX - b \tag{1. 1}$$

$$X = \left[\left(\frac{L}{D^*}\right)(\sin 2\alpha)^{0.5}\right]^{-0.1}\left[\left(1+\frac{1}{GLR}\right)^{0.25} - 1\right]\left[\frac{p_c}{239}\right]^{0.05} \tag{1. 2}$$

In these equations the variables a and b are experimentally determined coefficients while L/D^* is the length to diameter ratio of the mixing chamber and α is the converging angle after the mixing chamber. The values for a and b are listed in reference [4] for different setups. In addition to affecting the discharge coefficient the ratio of L/D^* also plays an important part in drop size. Figure 1-2 taken from reference [4] shows this effect. From Figure 1-2 it can be seen that as L/D* decreases so does the SMD. So it is desirable to decrease this ratio as much as possible if small droplets are desired.

Another important design parameter that affects the spray is the air injection holes. The parameter used to describe their effect is the ratio of the discharge orifice area to the total area of the air injection holes or A^*/A_a. This effect can be seen in Figure 1-3 taken from reference [4]. This figure shows the Sauter mean diameter (SMD) vs. the air to liquid mass ratio (ALR also GLR), and the dashed line shows the optimum ratio of

A^*/A_a. From this graph it can be seen that ideally A^*/A_a would increase as the ALR increased. This ideal relationship can be shown by Eq. 1.3.

$$\frac{A^*}{A_a} = 6.3ALR \tag{1. 3}$$

In contrast to standard injectors it was found that the droplet sizes did not depend on the injector exit diameter [3]. Figure 1-4 shows this effect. From this figure it can be seen that the only effect is coming from the varying GLR. The different injector diameters all correspond to the same droplet sizes.

The GLR is one of the most important variables that can affect the spray produced by an aerated injector. Its affect can be found in almost all of the derived correlations used for predicting different properties of the spray. The different GLR values can be characterized as bubbly flow, intermittent flow, and annular flow. Their effects can be seen from the work of Kim and Lee [5] and Lin et al. [6]. Kim and Lee [5] show the effect on drop size in Figure 1-5.

The bubbly flow regime occurs at a GLR range lower than approximately 0.004 depending on the diameter of the injector. It is characterized by the gas bubbles that are formed at the air injection locations traveling down and eventually exiting the injector (Figure 1-6). The droplet sizes in the bubbly flow regime are larger than those produced in the annular flow regime. This is due to the fact that larger ligaments are produced at the exit because of the thicker liquid film surrounding the bubbles than the thinner liquid film seen in the annular regime. Santangelo and Sojka [7] investigated these bubble structures at the exit of the injector using holography. They found that the bubbles

existed for a short time outside the injector where they expanded and eventually exploded creating droplets and ligaments (see Figure 1-7). These structures were described as tree-like structures having a trunk, limbs, branches, ligaments, and drops (see Figure 1-8).

The annular flow regime occurs at higher GLRs beginning around GLR = 0.02 depending on the injector diameter. This regime consists of a fully developed inner gas core surrounded by a thin liquid film (see Figure 1-9). This regime is characterized by much smaller droplets than the bubbly flow. It can also be seen in Figure 1-5 that the droplet sizes begin to converge and no longer behave as a function of injection pressure and injector diameter. This is due to the thin liquid sheet that is created by the annular regime shown with a thickness, δ in Figure 1-9. The droplet sizes are now controlled by this liquid sheet thickness. This allows small droplets to be produced from relatively large injectors. This makes the aerated injector a good candidate for fluids that are prone to clogging but still need the small droplets that would otherwise have to be produced with a smaller injector. Figure 1-5 also shows that after a certain point increasing the GLR has little or no effect.

In the intermittent regime the flow is switching between the bubbly and the annular flows. This causes a bimodal drop size distribution which was observed by Kim and Lee [5]. This bimodal distribution is caused by the droplets being produced by the two different breakup mechanisms of bubbly and annular flow.

The effects of the ratio between the injection pressure and the ambient pressure on drop sizes and cone angle were studied by Wade et al. [8] and Sovani et al. [9]. Wade et al. [8] studied this cone angle but the injection was done in atmospheric pressure. Sovani et al. [9] expanded this work by injecting into a range of ambient pressures. The

combined effects of ambient pressure and GLR were observed. They observed that the spray cone angle increased monotonically as the GLR increased. They also found that the cone angle increased as the injection pressure increased. These angles observed where also in the same range as sprays produced by conventional pressure atomized sprays. In this work they also observed a peculiar occurrence at the lower end of the ambient pressure region. Figure 1-10 shows that the cone angle vs. ambient pressure. It can be seen that the cone angle decreases as the ambient pressure increases in the beginning, but later the cone angle begins increasing with higher ambient pressure. This is thought to be because at lower ambient pressures the two phase flow is choked and it expands rapidly when it exits. Then as the ambient pressure is increased the flow becomes unchoked and the widening of the spray is due to the increased drag on the droplets due to increasing density [9].

The effect of ambient pressure on droplet sizes was studied by Chen et al. [10]. They found that as the ambient pressure was increased the droplet size increased and eventually peaked and then began to decline again (see Figure 1-11). This occurred because at lower ambient pressures extra energy comes from the bubbles inside the flow expanding. These bubbles eventually stop expanding due to the increased ambient pressure and then the droplet size increase is due to the rising Weber number [10].

Buckner and Sojka [11] studied the effects of viscosity on aerated injectors. Their work showed that the droplet size was a function of GLR only and the viscosity had no real effect on droplet sizes. This insensitivity to viscosity has promise in applications where low quality fuels are used and the viscosity cannot be controlled well. Similarly, applications can be found in waste incineration where viscosity varies widely [2]. In

contrast to their work Sovani et al. [2] states that the performance of the injector at higher injection pressures are strongly affected by viscosity, and that drop size increases with increased viscosity. More research needs to be done to determine when the viscosity begins having an effect. If it is true that the viscosity only begins affecting the spray at higher injection pressures then some type of cutoff value needs to be determined so that it will be known when the effects of viscosity should be considered.

Lund et al. [12] studied the effects of surface tension by mixing glycerin and water to achieve different surface tensions. They found that droplet sizes actually decreased with increasing surface tension. This was explained by a primary atomization model based on the instabilities within the fluid.

The jet-to-freestream momentum ratio or q, has been studied because of its effect on spray penetration height by Lin et al.[13-16]. It was found that the penetration height is a function of the GLR and q and that there was no real effect on the SMD from changing the q. They provided a correlation from to predict the penetration height given the GLR, Mach number, q, and x/d in Equation. 1.4.

$$(h - h_0)/d_0 = 0.9(GLR)^{0.46} M^{-0.64} q_0^{\,0.34} (x/d_0)^{0.39} \qquad (1.4)$$

From this equation it can be seen that as the GLR is increased the penetration height will also increase. This is due to the thin liquid film that is present in the annular regime being squeezed into a smaller thickness which increases its velocity. This effectively gives the spray a higher jet-to-freestream momentum ratio than the non aerated condition used to obtain q_0. This increased momentum ratio makes this type of injector desirable

for ramjet and scramjet engines where spray penetration is a problem due to the high speed crossflows. The aerated injector allows the combustion to occur farther away from the engine walls while the injection pressure requirements stay relatively small when compared to injection pressures needed to produce the same height with conventional injectors.

The fluid mechanics aspects of the aerated injectors are very complicated. Inside the injector there are two phases of fluid rapidly mixing to form some state of two-phase flow depending on the GLR, and outside the injector either bubbles are bursting forming droplets and ligaments or the thin liquid sheet present in the annular regime is breaking up. There has been some progress on developing some type of model that will predict the properties of a spray produced by an aerated injector. Lund et al. [12] provided a fundamental model based on instabilities within the flow. They first assumed that the flow at the exit of the injector consisted of an annular structure of a gas core surrounded by a liquid sheet. This liquid sheet thickness is then calculated and it is assumed that cylindrical ligaments are formed having the same diameter as the thickness of the liquid sheet. This model only represents primary breakup and secondary breakup is neglected. The equation provided by Lund et al. [12] predicts the SMD based on the l_d, μ_l, ρ_l, and σ_l (Eq. 1.5).

$$SMD \approx \left[\frac{3}{2} \sqrt{2} \pi d_l^{\,3} \left(1 + \frac{3\mu_L}{\sqrt{\rho_L \sigma_L d_l}} \right)^{1/2} \right]^{1/3} \tag{1.5}$$

This model does predict the SMD with a fair amount of accuracy but it is limited by the fact that it neglects aerodynamic effects due to the relative velocity between the ligaments and the ambient air. Sutherland et al. [17] improved this model by adding the effects of the relative velocity between the liquid and the ambient air. They also included some experimentally obtained coefficients to better improve their model. Theoretical results have also been obtained to model what is actually happening within the aerated injector. They have predicted the primary atomization well but still need work to fully describe the secondary breakup effects.

These previous studies have provided valuable information about the properties of the aerated injector but there is some information that is lacking. Specifically, there have been no studies on the dense spray area just downstream of the injector when injecting in a crossflow. The majority of the work has been at the injector exit or far downstream on the dispersed phase. There is a need to fill this gap to better understand what is happening between these two regions. This will require the development of advanced diagnostics capable of probing this optically challenging region.

1.3.2 Holographic Techniques

Holography relies on two beams of coherent light: 1) the object beam, which comes is diffracted by the object being recorded and 2) the reference beam, which represents what the object beam was like before it was affected by the object. When the object beam comes in contact with the object, the phase of the light is changed so that when it comes in contact with the reference beam an interference pattern is formed which can be recorded. This interference pattern is the hologram itself. If the original reference

beam is shone onto the hologram then a 3-D image is reproduced having the same characteristics of the original object. This technique was first invented by Gabor [18] in 1948 and later it was improved by Leith and Upatnieks in 1962 with the addition of the off-axis reference beam, which separated the real and virtual image. With the advancements in computer technology, Goodman and Lawrence [19] found that holograms could be recorded on film and reconstructed digitally. Later with the development of the CCD sensor, Schnars and Juptner [20] recorded and reconstructed holograms entirely digitally.

Two beams are still needed in digital holography, but they can be within the same beam. This works because if there are portions of the beam that are unaffected by the object then they can serve as the reference beam. This single collimated beam setup is preferred over other possible holographic recording methods because of its simplicity and its favorability to digital recording. The inline arrangement reduces the spatial resolution requirements on the CCD sensor which has a much lower resolution than traditional holographic film. The interference of the object and reference beam creates light and dark fringes, and according to the sampling theorem each fringe has to fall across two pixels to be resolved. The frequency of these fringes increases as the angle between the object and reference beam increase. Therefore, the in-line arrangement is the most suitable for the lower resolution CCD sensors. In addition to its lower resolution requirements there is not a need to match the lengths of the optical paths of two beams to stay within the coherence length of the laser, and this simplifies the experimental setup.

The principle drawback with this single beam setup is that resolution decreases in a dense spray because there is not enough of the beam that passes through the volume

unaffected by particles to serve as a reference beam. The Royer criterion [21] quantifies this amount of obscuration based on “shadow density.” According to the Royer criterion, hologram quality can be defined by: a shadow density less than 1% produces a "good" hologram, between 1% and 10% produces a "marginal"-quality hologram, and greater than 10%, a "bad" hologram. Adding a separate reference beam solves the beam obscuration problem. However, to keep the low fringe frequency both the object and reference beam are combined with a beam splitter and sent to the CCD with in-line configuration.

This addition of a separate reference beam solves the problem of beam obscuration, but it does not solve all the problems associated with recording dense sprays. Another problem is intrinsic speckle noise. Meng et al. [22] describes this speckle noise as the interference of the scattering waves from multiple particles. When the scattered light waves interfere with each other, they appear as a random pattern of speckles when the hologram is reconstructed. This causes a problem with automatic particle measurement because it becomes difficult to distinguish a focused droplet from the speckles. Meng et al. [22] offers two ways to improve this problem: 1) suppress the undiffracted reconstruction wave (a.k.a dc term) and 2) Separate the virtual and real image through an off-axis setup. Schnars and Jueptner [23] offer two simple ways of suppressing this DC term: 1) subtract the average intensity from the hologram or 2) measure the intensities of the reference beam and object beam separately and subtract the intensities from the hologram before reconstruction.

As for the virtual image issue, Meng and Hussain [24] provide a novel way for keeping the simplicity of the in-line recording configuration, and still have the benefits of

off-axis reconstruction. However, this has only been done optically and to this author's knowledge has not been implemented digitally.

Digital holographic microscopy is similar in setup to standard in-line digital holography except no lens is used to collimate the beam. This method eliminates the need for a relay lens to introduce magnification because the expanding beam provides the magnification needed. This eliminates two lenses from the optical path, which results in a much cleaner hologram recording and reconstruction. The expanding beam also increases the resolution system because the fringes that are needed to reconstruct the image are expanding with the light beam. This allows for recording distance to be shortened which results in higher resolution.

1.4 Specific Objectives

In view of the recent findings about the breakup of aerated liquid jets in crossflow, the specific objectives of this study were as follows:

1. Develop a technique that provides visualization and measurement of droplets in the dense near injector region, and automate it as much as possible for data collection.
2. Complete new measurements of the spray structures for aerated liquid jet in crossflow in the near-injector region that is currently opaque to PDPA techniques at x/d = 25 and x/d =50.
3. Investigate the effects of GLR, Injector exit diameter, and jet-to-freestream momentum ratio on the spray structure.
4. Use phenomenological analyses to interpret the new measurements of the properties of the breakup of aerated liquid jets in crossflow.

1.5 Organization of the Thesis

The thesis is organized into four chapters and two appendixes. The first chapter has covered background, the problem statement, previous studies, and the specific objectives. The second chapter will cover the experimental setup and the measuring techniques used. Then the third chapter will cover the results of the study looking at the effects of GLR, jet diameter, jet-to-freestream momentum ratio, and downstream location. Finally, the fourth chapter will go through the conclusions of the study and recommend future work to be done. The first appendix contains extra figures showing the results of the measurements and the second contains all of the measurements.

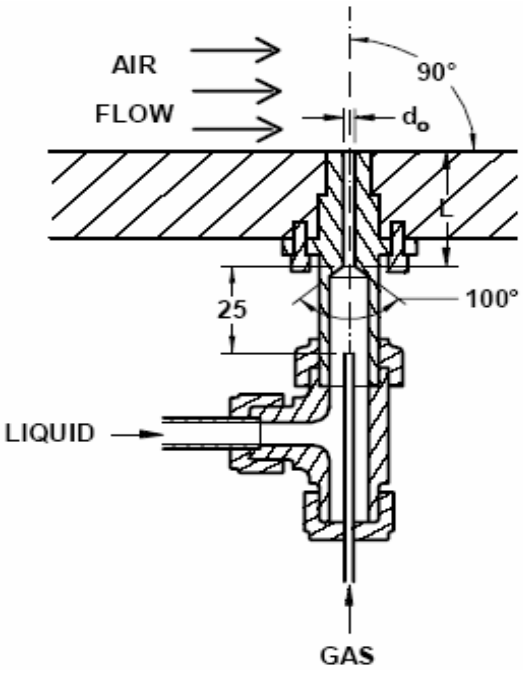

Figure 1-1 Schematic of an aerated injector (inside out setup shown) (from reference [15]).

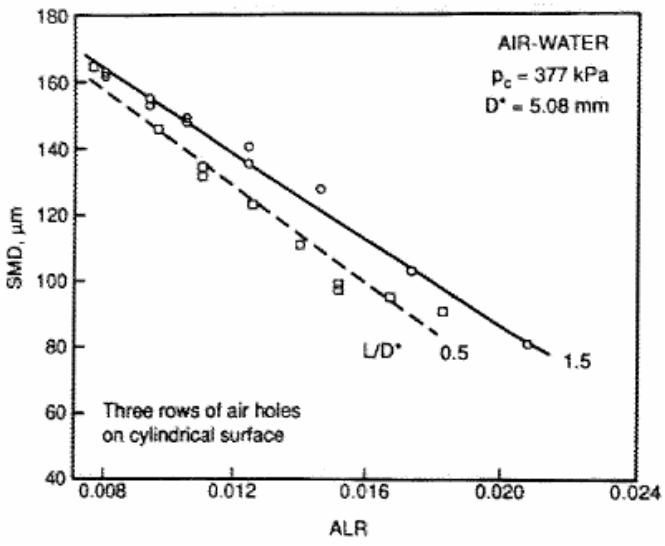

Figure 1-2 Effect of L/D^* (from reference [4]).

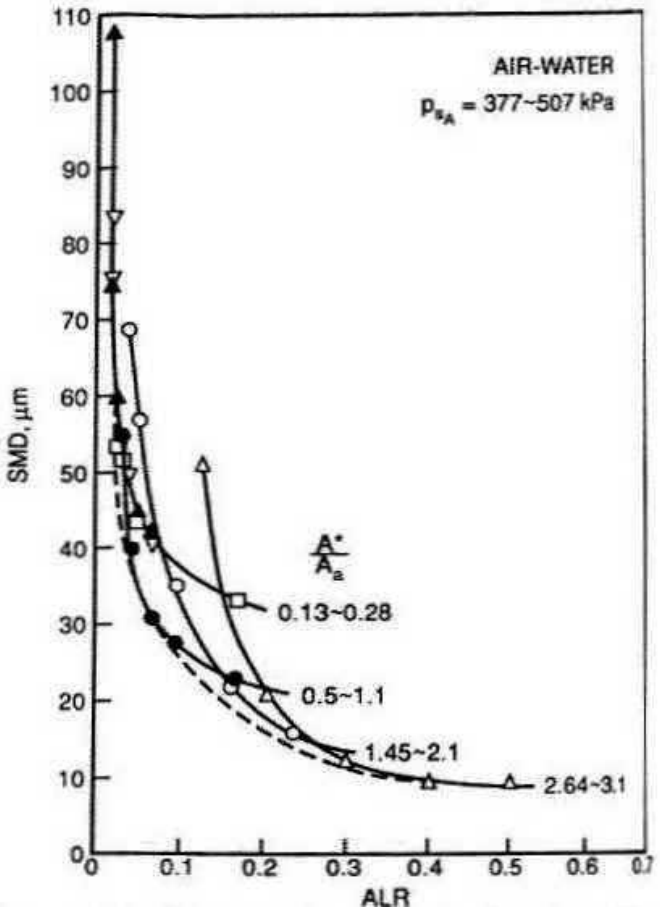

Figure 1-3 Effect of A^*/A_a (from reference [4]).

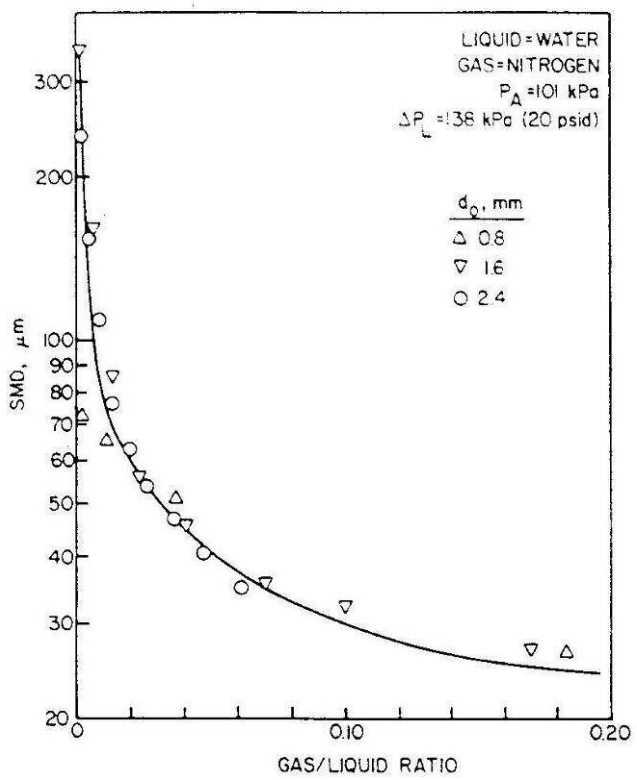

Figure 1-4 Effect of jet diameter on droplet size (from reference [3]).

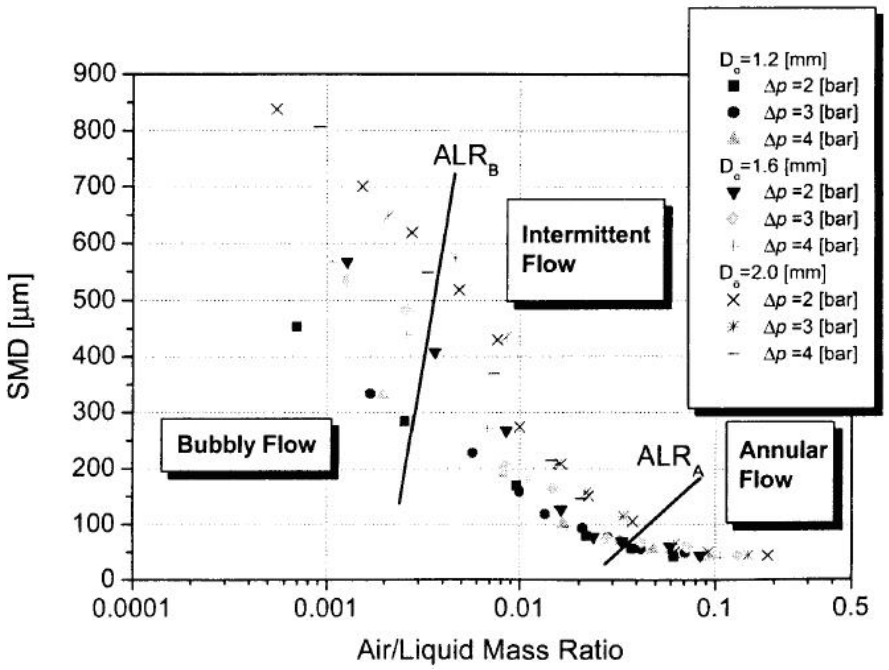

Figure 1-5 Drop sizes vs. air-liquid mass ratio (from reference [5]).

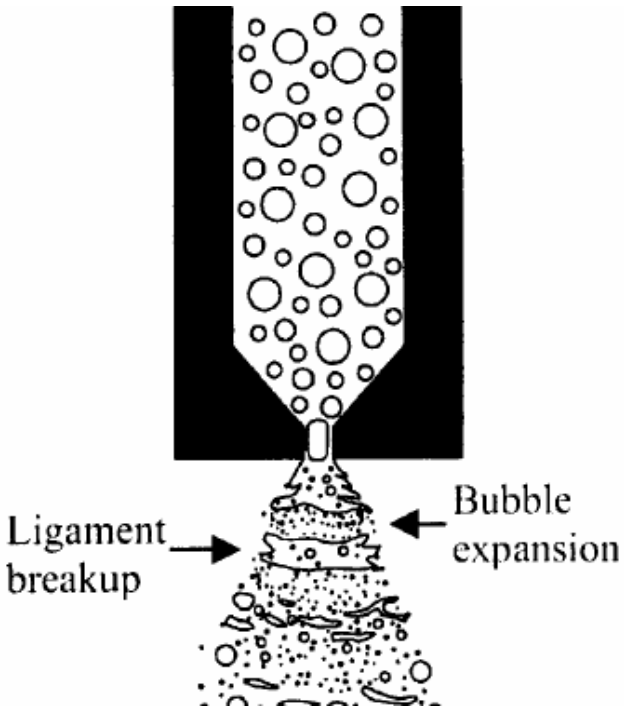

Figure 1-6 Sketch of the bubbly flow regime (from reference [7]).

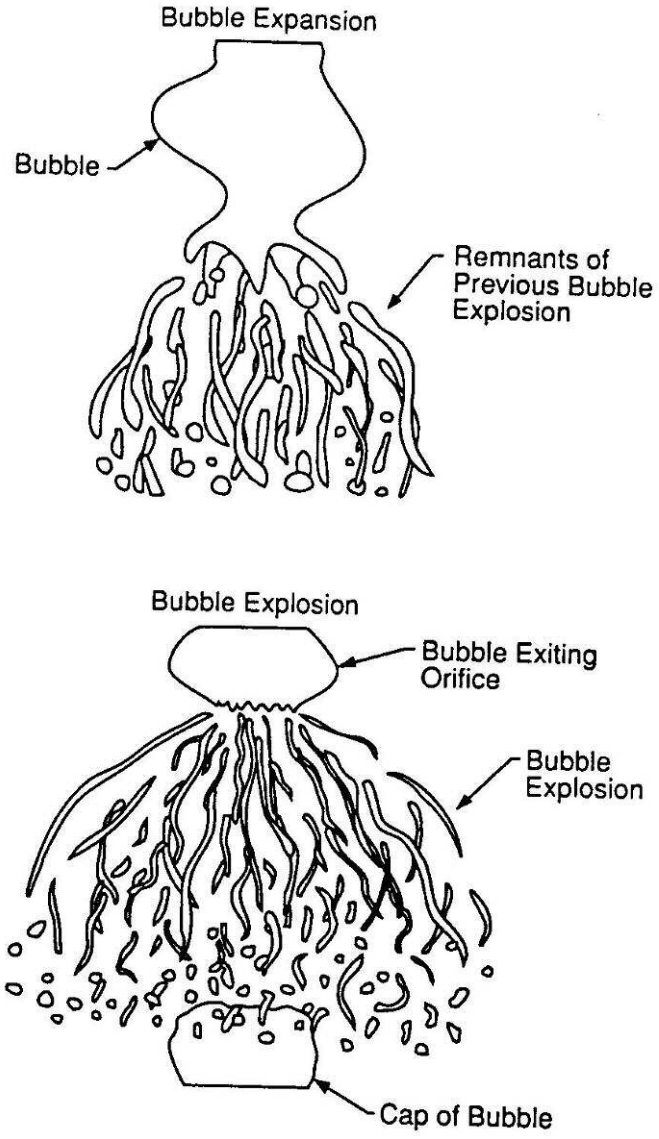

Figure 1-7 Sketch of the bubble structure near injector exit (from reference [7]).

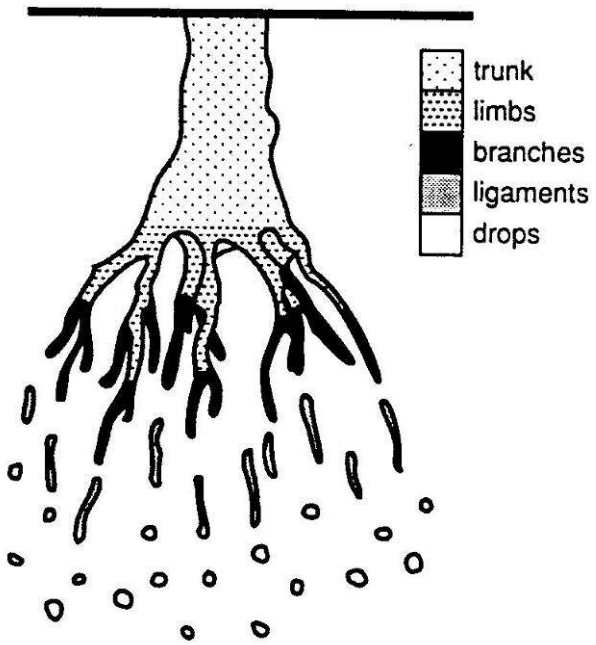

Figure 1-8 Sketch of the tree structure at injector exit (from reference [7]).

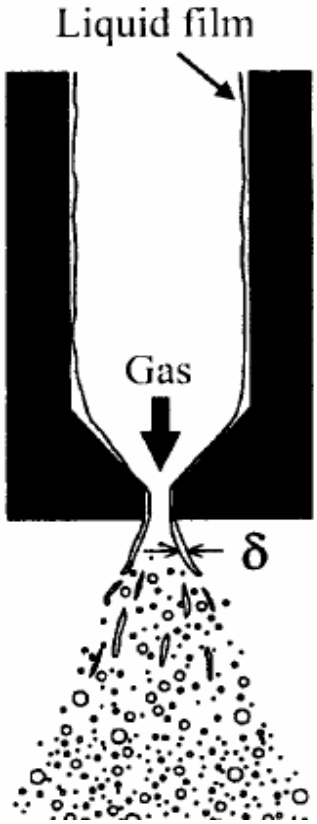

Figure 1-9 Sketch of the annular flow regime (from reference [7]).

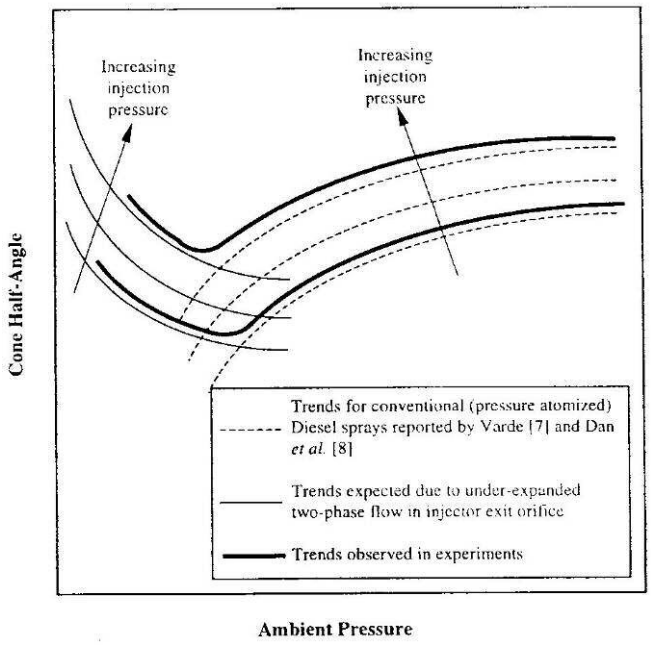

Figure 1-10 Cone angle vs. ambient pressure (from reference [9]).

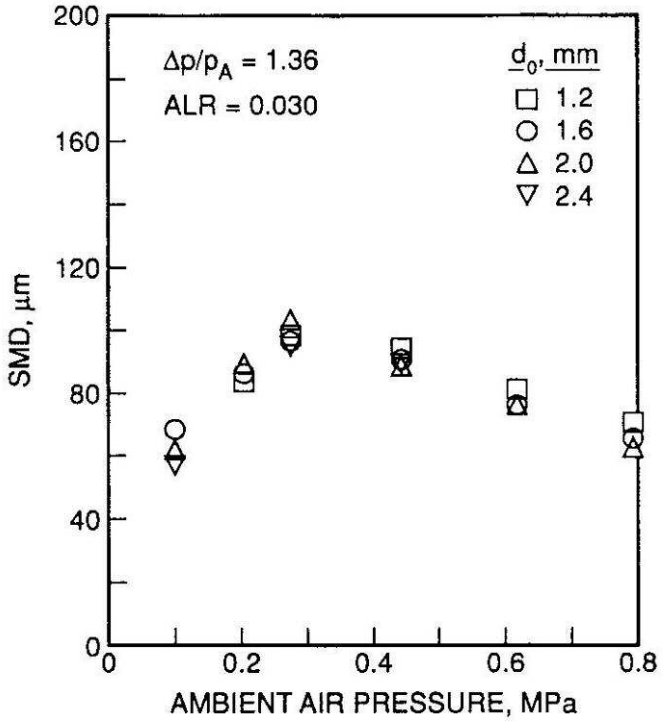

Figure 1-11 Effect of ambient air pressure on SMD (from reference [9]).

Chapter 2.

Experimental Method

2.1 Introduction

This chapter introduces the equipment and methodology used to carry out the experimental investigation.

2.2 Test Apparatus

The aerated liquid jet breakup experiments were carried out in a subsonic wind tunnel with a test section of 0.3 m x 0.3 m x 0.6 m. The wind tunnel had float glass side walls and floor, and acrylic ceiling to provide optical access. Possible air velocities were in the range of 3-60 m/s at normal temperature and pressure. The air velocities in the test section were in the range of 3-60 m/s at normal temperature and pressure. The air velocity in the test section, was measured by a Pitot-static tube (United Sensors Model PDC-18-G-16-KL) installed at the end of the test section. The pitot static tube was connected to an inclined tube manometer (Dwyer Model No. 400-10-Kit) through two clear plastic tubes. The wind tunnel had a contraction ratio greater than 16:1 and the velocity variation inside the test section was $< \pm$ 1% of mean free-stream velocity. Air velocities in the wind tunnel could be measured within +/- 2%.

Aerated-liquid injectors with exit diameters of 0.5 mm and 1.0 mm were used. These injectors consist of an inner tube for the aerating gas and an outer tube for the

liquid, as shown in Figure 1-1. The test liquid was contained within a cylindrical liquid supply chamber having a diameter of 100 mm and a length of 300 mm, constructed of type 304 stainless steel. The liquid was forced through the injector by admitting high-pressure air to the top of the chamber. The aerating gas travels through the inner tube and passes through several 100 μm holes located near the end of the tube. At sufficient GLRs (greater than 2%) the gas and liquid mix to form a two-phase flow which consists of a gas core surrounded by a thin liquid sheet (annular regime). The air and liquid flow rates were then controlled by rotameter type flow meters (air flow meter: OMEGA model # 044-40NCA, water flow meter: OMEGA model # N034-39G). The air flow meter could read flow rates +/- 3 cc/s and the water flow meter could read flow rates +/- 0.02 cc/s. Therefore, the maximum uncertainty in the gas flow rate measurement is 28% and the maximum uncertainty in the liquid flow rate measurement is 6%. The high-pressure air was kept in a storage tank with a volume of 0.18 m^3 and provided an injection pressure at 1.1 MPa.

2.3 Instrumentation and Measuring Techniques

Digital holography was chosen because it is unaffected by the non-spherical droplets that are encountered very close to the injector exit, which causes problems for techniques such as PDPA. It also works well for observing the very dense spray conditions that are encountered just downstream of the injector exit. Two different methods of digital holography were used in the present study. The first was in-line digital holography, which relied on the use of either one collimated beam falling directly on the CCD sensor, or two collimated beams which were combined with a beam splitter

and sent to the CCD in an inline configuration. The two beam setup was used when the spray was dense and blocked a majority of the collimated beam passing through the spray. The other technique used was digital holographic microscopy which uses one expanding beam falling on the CCD in an in-line configuration. This method provides higher resolution allowing smaller droplets to be seen. However, this method does come at the cost of reduced recording distances.

2.3.1 In-Line Digital Holography

In-line digital holography was chosen because of its ability to capture a large field of view and its experimental setup simplicity. However, this technique would not provide the resolution needed to resolve the smallest droplets in the spray. For higher magnification, but smaller field of view, digital holographic microscopy was used. This technique removes some of the lenses that were necessary in the in-line setup which greatly reduces the number of aberrations introduced by lenses. Using digital holographic microscopy, three dimensional maps were made of the SMD distribution of the sprays at different conditions. From these SMD plots different parameters can be investigated such as the effects of changing GLR, jet exit diameter, jet/freestream momentum flux ratio, and different downstream distances.

The optical setup consisted of two frequency doubled YAG lasers (Spectra Physics Model LAB-150, 532 nm wavelength, 7 ns pulse duration, and up to 300 mJ optical energy per pulse with injection seeder to increase the coherence length of the laser light. The beams were combined using a polarized beam splitter cube. The resulting beam then passed through another polarized beam splitter cube, which only allows either

the horizontal or vertical portion of polarized light to pass through while the other portion is reflected and directed to a beam dump. This combination of half wave plates and beam splitter cubes controls the intensity of the beam. The beam then passed through another half wave plate and polarized beam splitter cube to split the beam into object and reference beams. The reference and object beams then passed through a series of mirrors for positioning, and then passed through two 20x objective lenses and 3 inch diameter convex lenses with focal lengths of 150 mm. The object beam then passed through the test section and fell directly on the CCD (see Figure 2-1), while the reference beam passed under the test section and was then directed back up to the CCD and combined with the object beam by a beam splitter. The magnification was introduced by using a convex lens with a focal length of 300 mm as relay lens after the test section, and the magnified hologram was then captured by the CCD.

After the hologram is recorded, it is reconstructed using a MATLAB program based on the convolution type approach which solves the Rayleigh Sommerfeld formula for reconstruction of a wave field. This is done with the use of the Fast Fourier Transform algorithm [25]. This convolution method was chosen over the other popular and faster method using the Fresnel approximation because according to Kreis et al. [25], with the Fresnel approximation the reconstructed pixel size depends on the wavelength of the light and the reconstruction distance.

The method of average intensity subtraction is used in the current setup to suppress the DC term when reconstructing the hologram, and the current setup neglects the out of focus virtual image because its effect is small enough that droplets can still be resolved and measured accurately.

The results of this method can be seen in Figure 2-5 and Figure 2-6. This method works very well for capturing the large details of spray because of its large field of view. Figure 2-5 shows the original image and Figure 2-6 shows the reconstruction. However, when the smaller details need to be examined a relay lens must be introduced to provide magnification. This works adequately for low levels of magnification but aberrations in the relay lens begins to become a problem at higher levels of magnification. Figure 2-3 shows a reconstruction of a resolution target that was recorded using this method and the aberrations introduced from the relay lens can be seen clearly. The noise in this image poses a large problem for an automatic drop detection algorithm which is based on the intensity gradient within the image.

In order to apply physical dimensions to the images a calibration must be made to determine what length each pixel represents. In ordinary 2-D techniques an image of an object of known dimensions would be captured and a calibration could be applied. This same technique can not be used for a 3-D hologram using magnification because objects closer to the relay lens appear larger than those farther away. To solve this problem many calibration images were captured of a resolution target (Figure 2-4) placed at different distances from the camera. This results in different length/pixel calibrations at different distances from the camera. These different values can be plotted vs their distance from the camera and a line can be fitted through these points giving a calibration equation for any distance from the camera. Using these calibration images it was found that objects as small as 12 μm could be resolved. This was adequate to measure the droplets in the spray with SMDs on the order of 100 μm.

2.3.2 Digital Holographic Microscopy

For the holographic microscopy approach much of the same setup as described above was used except only one beam was used that was expanded with a 5x objective lens, and then it passed directly through the test section to the CCD. All of the holograms were captured on a Cooke Corporation cooled interline transfer CCD camera (Cooke, Model: PCO 2000) having 2048 x 2048 pixels that were 7.4 μm wide by 7.4 μm tall. All holograms and 2-D images were reconstructed and analyzed using MATLAB® combined with the optional image processing toolbox.

Magnification can be introduced during the reconstruction after the hologram has been recorded. This is done by manipulating the equations used in reconstruction. The manipulation comes in the form of relocating the virtual source point used in reconstruction. However, this does not improve the actual resolution of the image. The actual resolution is controlled by the distance from the object to the CCD, the wavelength of the light, and the pixel size of the CCD. The equation for the resolution is given by Schnars and Jueptner [23] (Eq. 2.1).

$$\Delta\xi = \frac{\lambda d}{N\Delta x} \tag{2.1}$$

Where $\Delta\xi$ (μm) is the resolution, λ (μm) is the wavelength of the light, d (μm) is the recording distance from the object to the CCD, N is the number of pixels, and Δx (μm) is the pixel size. The magnification introduced in the program only serves to make the reconstruction larger. The resolution is still determined by Equation 2.1. The setup used in this study had typical resolutions on the order of $\Delta\xi$ = 10 μm. Figure 2-4 shows the

reconstruction of the same resolution target that was recorded in Figure 2-3 using the in-line method. The difference between the two methods can be seen clearly.

2.3.3 Droplet Detection

After the holograms have been reconstructed digitally, the result is many 2-D images which represent "slices" of the 3-D spray volume. In these images there are many droplets focused at different distances throughout the spray. Before any measurements can be made it must be determined which plane the droplet is focused in. It was found that the plane of focus for each droplet is characterized by having the lowest average intensity of all the 2-D slices. This is done by placing a window over the area of interest, in this case an area slightly larger than the droplet, and then averaging the intensity values of each pixel contained within the window. This is done for all of the 2-D images and sent to a chart such as Figure 2-10. The peak value of the lowest intensity on the chart can be used to determine or even predict in which plane the droplet will be focused.

After a focused droplet is found, a user made MATLAB measurement program is used that automatically outlines the droplet and measures its dimensions. Droplet edge detection in these reconstructed holograms is difficult because the backgrounds of these focused images are generally non-uniform due to other droplets at other planes that are out of focus. To correct these uneven backgrounds the average intensity of neighboring pixels was taken and then subtracted from the original image. This left only the focused droplets with a much more uniform background. Then the edges of the droplets can be located and outlined. This outlining process uses an intensity gradient method that assumes the edge of the droplet is at the location of the largest intensity gradient. The

pixels in this outlined region are counted, and properties such as cross-sectional area and a droplet diameter based on the cross-sectional area are calculated. Then actual droplet diameter can be calculated using the calibration procedure described in section 2.3.1.

Using this method the smallest droplets with diameters of 17 μm were measured with uncertainties of 50%. However, the majority of the droplets measured were near the SMD size. The smallest SMD size was 59 μm. Droplets of this size could be measured with uncertainty of 15%. Uncertainty in locating droplets in the z direction depends on how well the droplet's plane of focus can be found. Since reconstructions were made with 1 mm increments, the location of the centroid of the droplet can be known within +/- 1 mm. Measurements in the x and y direction were determined by the placement of the camera when the holograms were recorded. The placement of the camera could be determined +/- 2 mm.

2.3.4 Flow Visualization

In addition to the holograms recorded downstream, holograms were also recorded at the jet exit for flow visualization. The recorded hologram can be seen in Figure 2-5, and the reconstructed image at the plane of focus can be seen in Figure 2-6. From these images the gas core structure can be seen clearly. A comparison can also be made between the two holographic methods by comparing Figure 2-7 taken with in-line digital holography at the injector exit in a crossflow with the hologram recorded using digital holographic microscopy in Figure 2-8 and its reconstruction in Figure 2-9. The improvements between the two methods can be seen.

A sample of the holograms that were recorded downstream can be seen in Figure 2-11. The reconstructed image shown in Figure 2-12 shows the droplets in focus at the outer edge of the spray. The reconstructed images that are focused on the outer edges of the spray show much larger droplets when compared to the images of the inner portion of the spray which contain only a few small droplets. All of the holograms recorded in the downstream area were recorded using the digital holographic microscopy method described in section 2.3.2 so that the smallest droplets could be measured.

2.4 Test Conditions

Two aerated injectors were tested with exit diameters of 1 mm and 0.5 mm. These were then tested at two different GLRs of 4% and 8%. The aerating gas used was air pressurized to 1.1 MPa and the liquid used was tap water also pressurized to 1.1 MPa. The properties of the water were as follows: density = 999 kg/m^3, surface tension = 0.00734 N/m, kinematic viscosity = 1.12 E -6 m^2/s. The aerated-liquid jet was then injected into crossflows different speeds so that there would be two different jet/freestream momentum flux ratios of q_0 = 0.74 and q_0 = 4. Holograms were then recorded using the digital holographic microscopy setup at two different downstream distances of 25 and 50 jet diameters . At each of these locations holograms were recorded starting at the top of the test section and then moving the CCD sensor and the objective lens down in 15 mm increments which is the height of the CCD sensor. The sensor continued to be lowered until no more droplets appeared. The test conditions may be found in Table 2-1 and Table 2-2. Testing at this combination of conditions resulted in a total of 16 different sets of results. After the holograms were recorded, they were

then reconstructed in 1 mm increments throughout the spray volume. In each of the reconstructed images the focused droplets were measured and diameter and location were recorded for each individual droplet. The SMD was then calculated by averaging the values of the droplet diameters over three reconstructed images which is the equivalent of 3 mm.

d_0 (mm)	0.5	0.5	0.5	0.5	0.5	0.5	0.5	0.5
U_∞ (m/s)	56	56	24	24	56	56	24	24
M (-)	0.16	0.16	0.07	0.07	0.16	0.16	0.07	0.07
x/d_0 (-)	25	25	25	25	50	50	50	50
q_0 (-)	0.74	0.74	4	4	0.74	0.74	4	4
GLR (%)	4	8	4	8	4	8	4	8
$Q_{L,injected}$ (cc/s)	0.33	0.33	0.33	0.33	0.33	0.33	0.33	0.33
$Q_{G,injected}$ (cc/s)	10.8	21.7	10.8	21.7	10.8	21.7	10.8	21.7

Table 2-1 Summary of test conditions for 0.5 mm injector

d_0 (mm)	1.0	1.0	1.0	1.0	1.0	1.0	1.0	1.0
U_∞ (m/s)	61	61	26	26	61	61	26	26
M (-)	0.18	0.18	0.075	0.075	0.18	0.18	0.075	0.075
x/d_0 (-)	25	25	25	25	50	50	50	50
q_0 (-)	0.74	0.74	4	4	0.74	0.74	4	4
GLR (%)	4	8	4	8	4	8	4	8
$Q_{L,injected}$ (cc/s)	1.45	1.45	1.45	1.45	1.45	1.45	1.45	1.45
$Q_{G,injected}$ (cc/s)	49	103	49	103	49	103	49	103

Table 2-2 Summary of test conditions for 1.0 mm injector

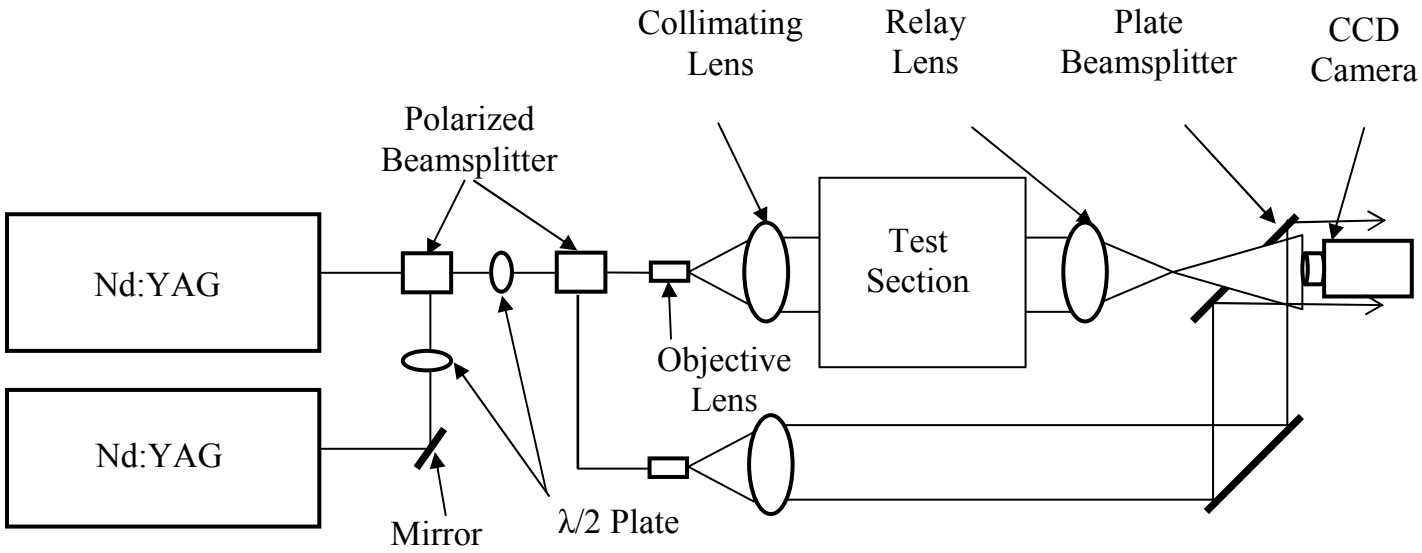

Figure 2-1 In-line digital holography setup with additional reference beam

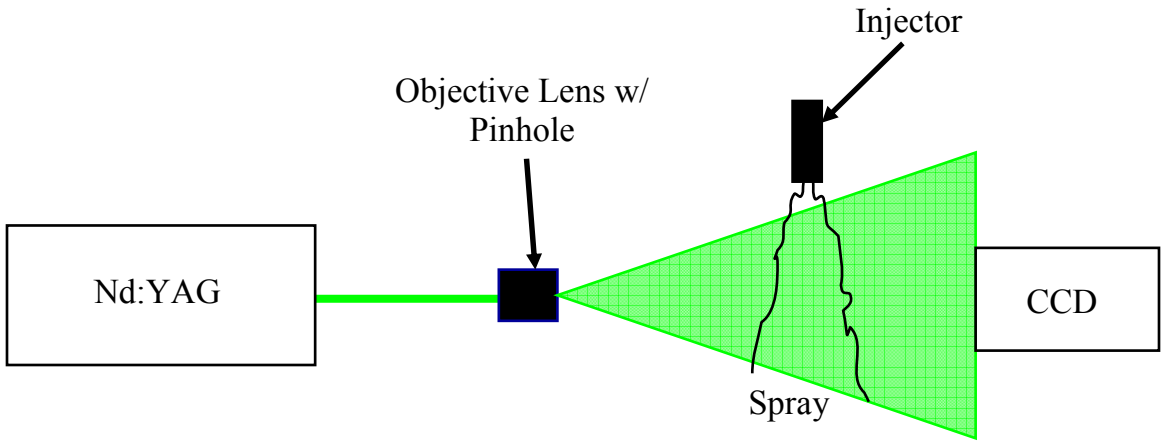

Figure 2-2 Digital holographic microscopy setup

Figure 2-3 Reconstruction of a Resolution Target using the Digital In-Line Holographic Method with Magnification from a Relay Lens

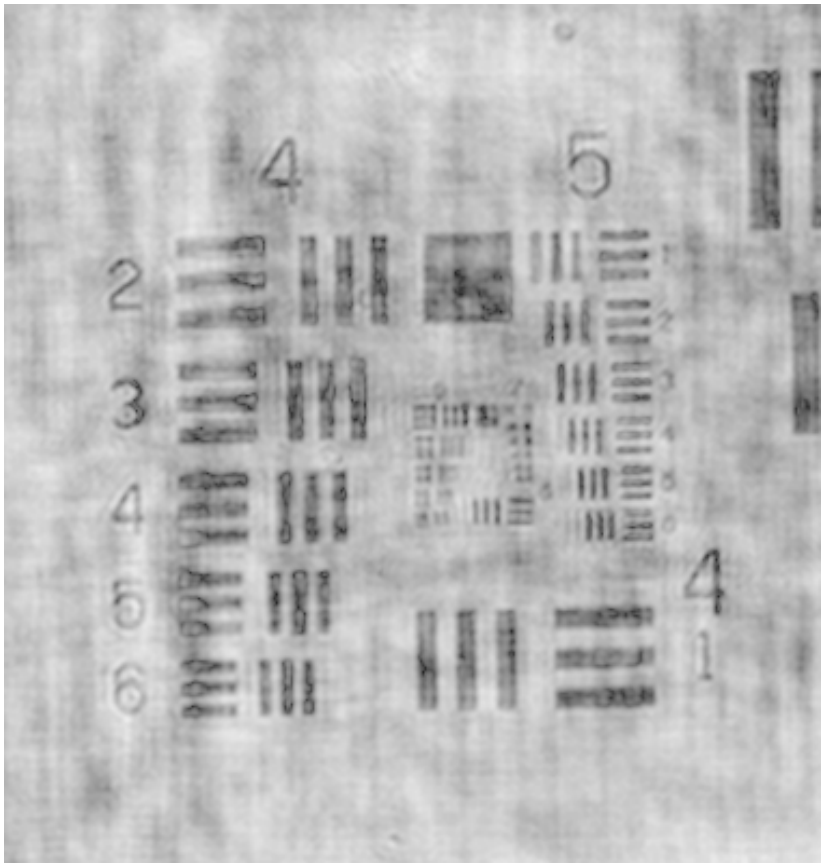

Figure 2-4 Reconstruction of a Resolution Target using Digital Holographic Microscopy Method

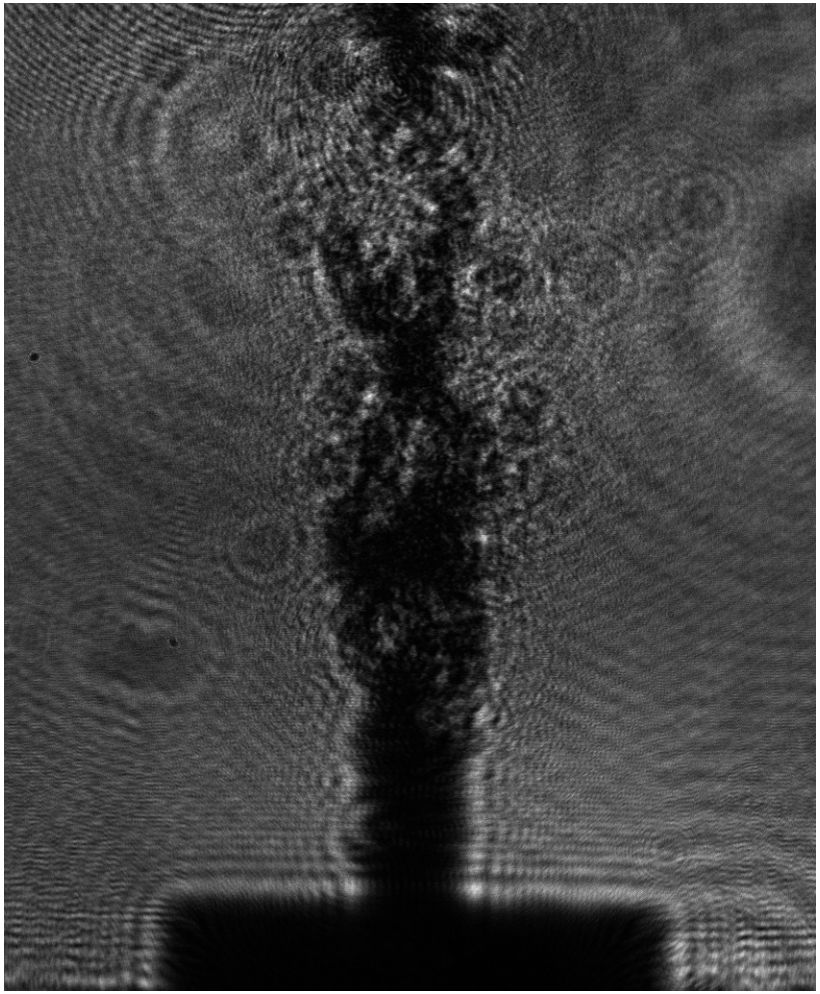

Figure 2-5 Digitally Recorded Hologram of Jet Exit at 2% GLR in Still Air

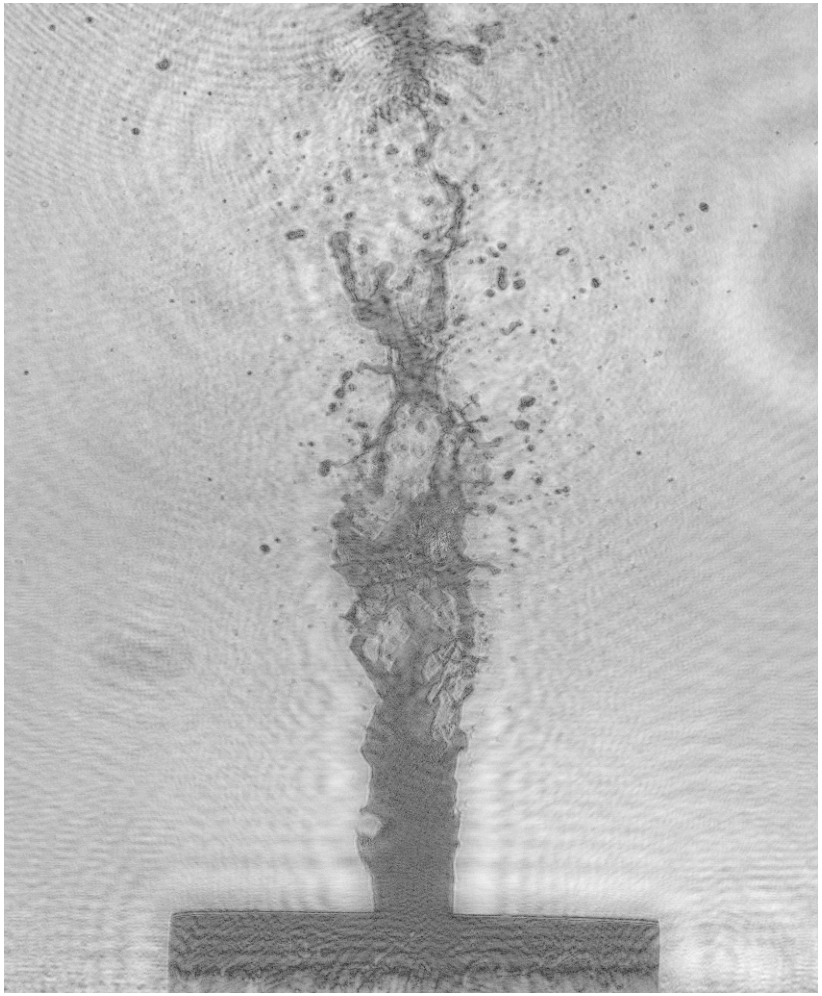

Figure 2-6 Digital Reconstruction of Jet Exit at 2% GLR in Still Air

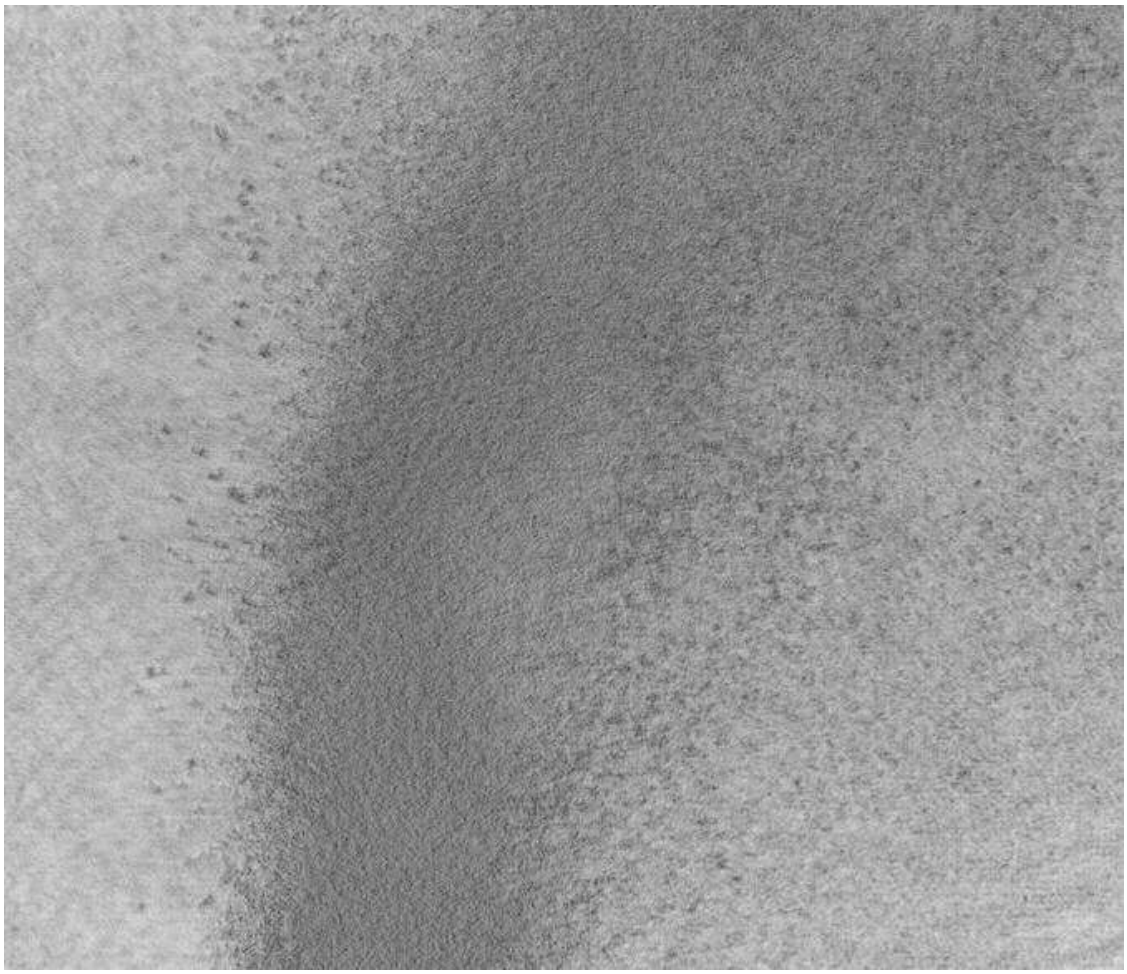

Figure 2-7 Reconstructed Hologram of Aerated Jet at 8% GLR in M=0.27 crossflow.

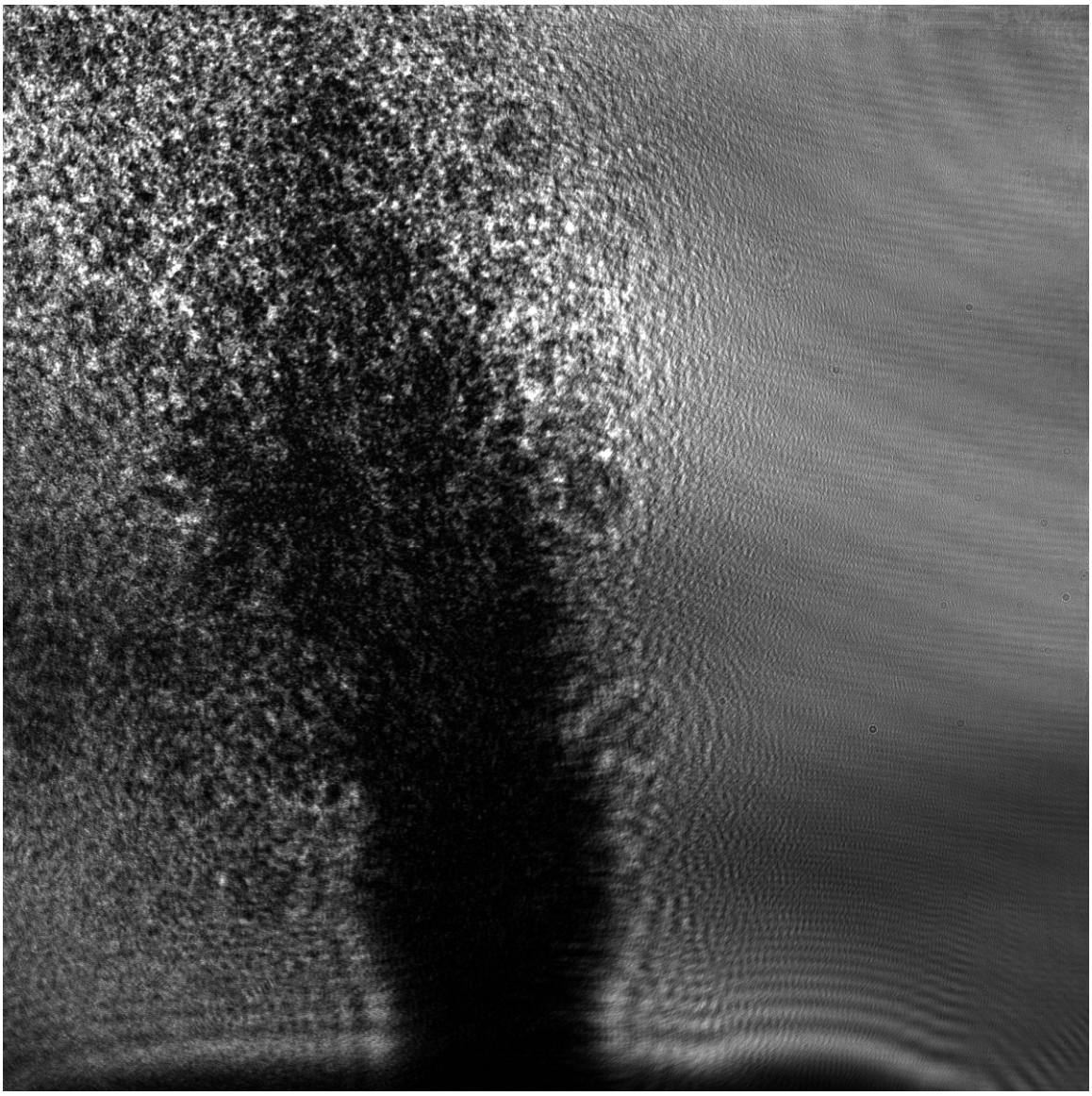

Figure 2-8 Hologram recorded using DHM taken at injector exit with conditions of GLR=4%, q_0=0.74, and d_0=1 mm.

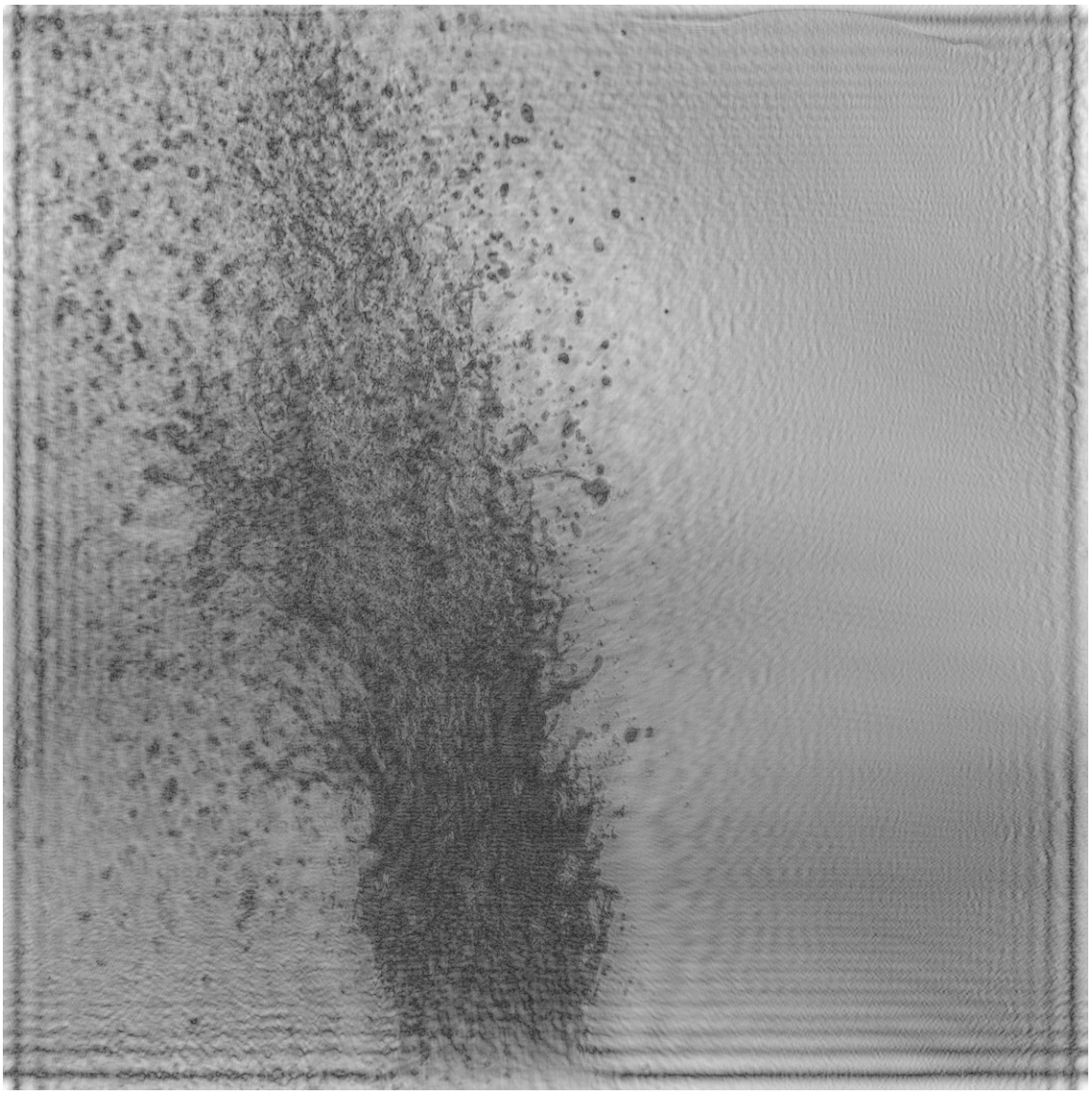

Figure 2-9 Reconstruction of Figure 2-8 at plane of focus.

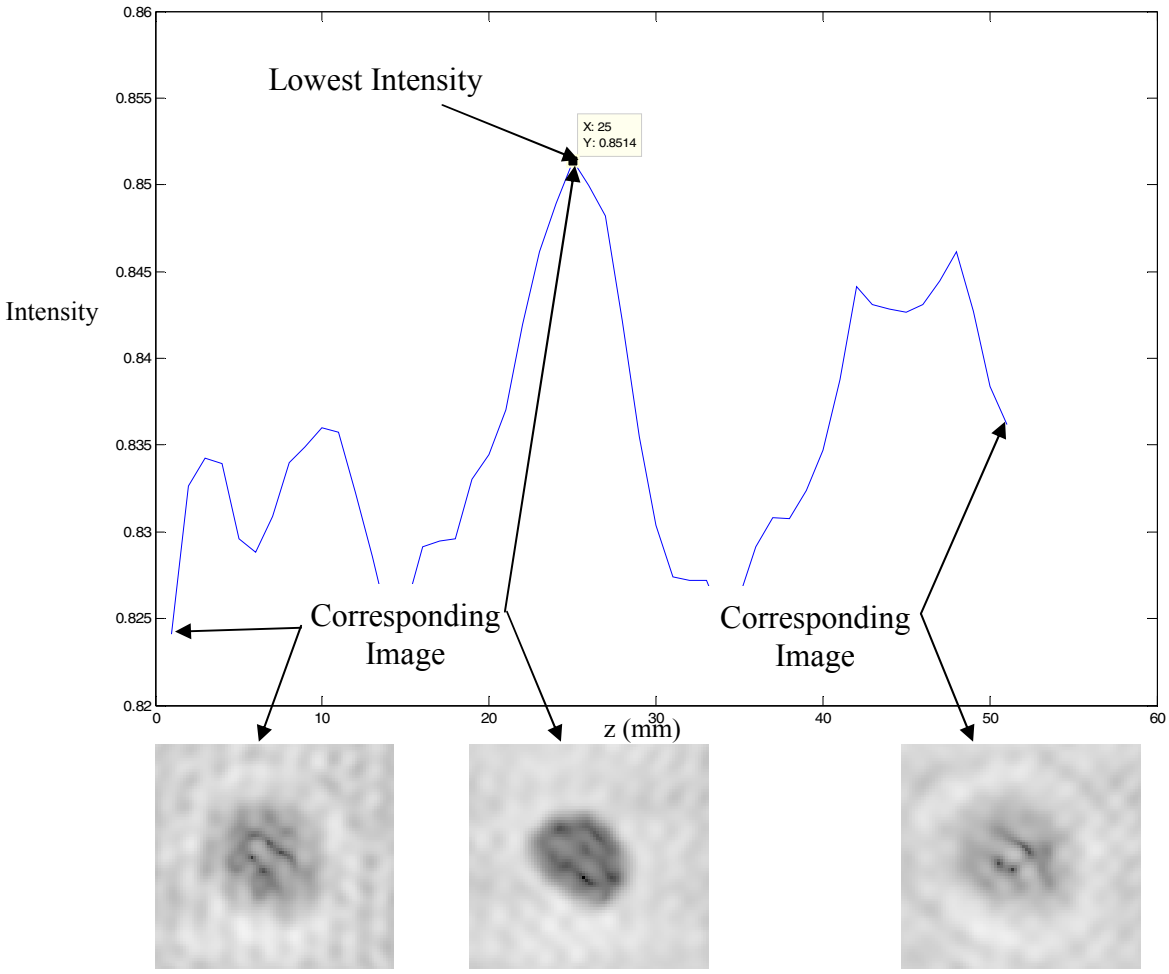

Figure 2-10 Graph of intensity versus distance in the z-direction and the corresponding images at different locations

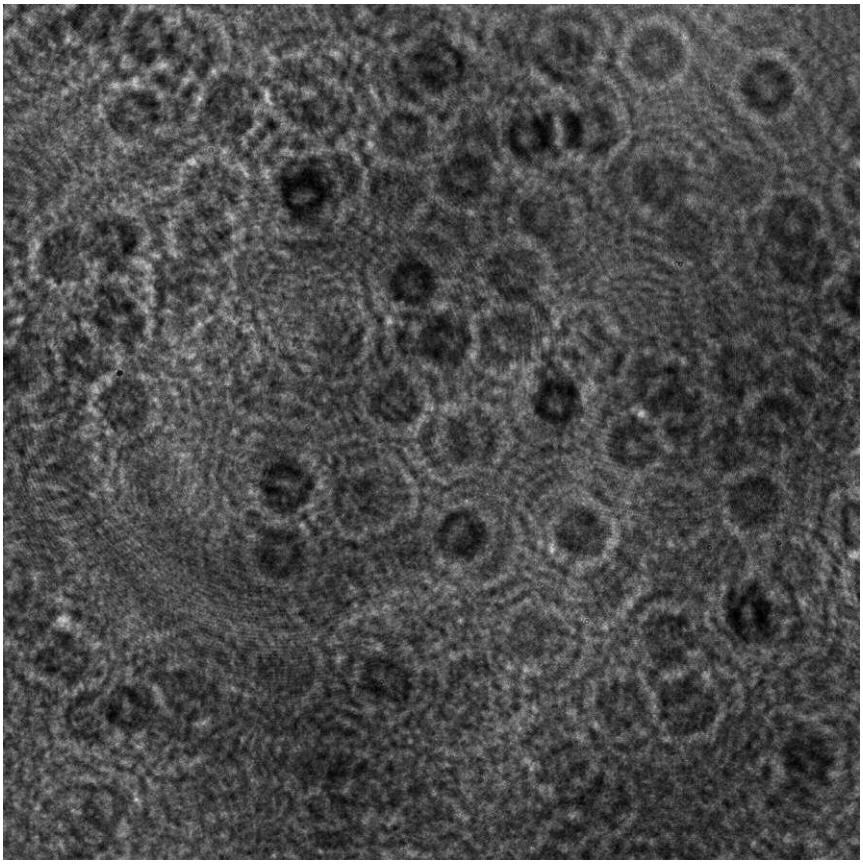

Figure 2-11 Digitally Recorded Hologram at x/d_0=25, GLR=4%, q_0=0.74, y/d_0=30, and d_0=1 mm

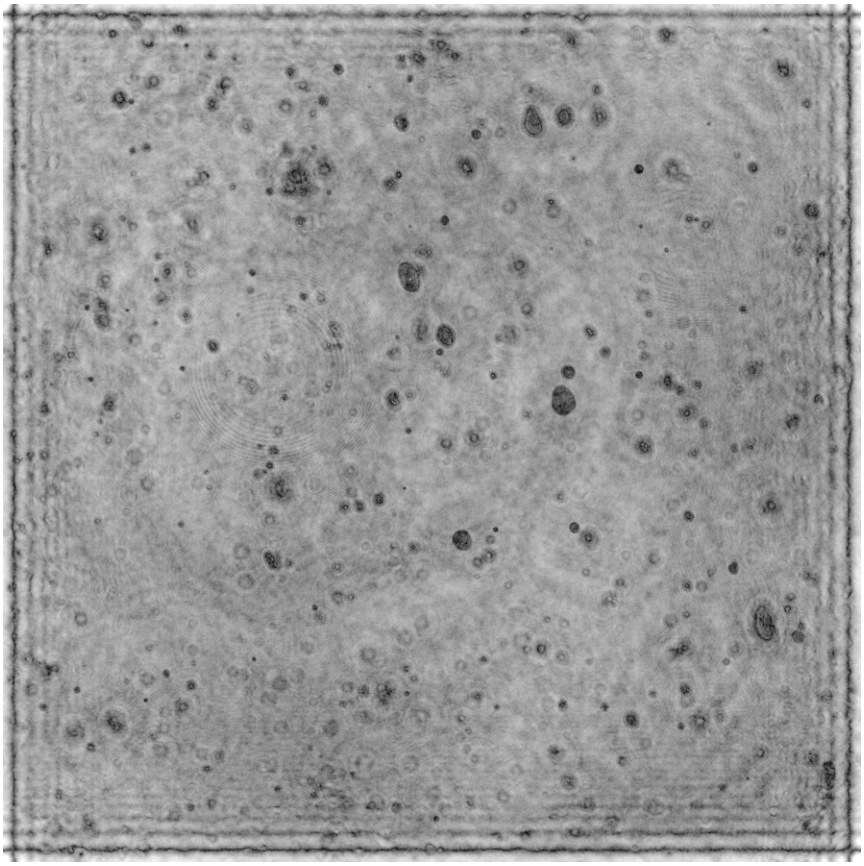

Figure 2-12 Reconstruction of Figure 2-11 focused at $z/d_0=6$

Chapter 3.

Results and Discussion

3.1 Introduction

Droplet diameters and locations were measured at the two downstream locations of x/d = 25 and 50 for each of the test conditions listed in Table 2-1 and Table 2-2. This resulted in a total of 16 different SMD distributions shown in Figures 3-2 through 3-6. The orientation of Figures 3-2 through 3-6 can be seen in Figure 3-1. The SMD values are represented by both the color and the actual size of the representative spheres in the plots. The effects of GLR, injector diameter, jet-to-freestream momentum ratio, and downstream location can be seen by observing the changes in these SMD distributions, volume fraction plots, and cumulative volume plots. Major changes in drop sizes are indications that secondary breakup is occurring. The present measurements fill the gap in the literature of spray structures of aerated jets in a crossflow between the upstream injector exit location [6, 7, 26] and the far downstream location [2-4, 8, 9, 11-16, 27-30].

3.2 Effect of GLR

Changing the GLR had the most effect over the droplet sizes. Figure 3-2 shows this effect. The SMD for the entire population at the condition of d_0 = 1 mm and q_0 = 0.74, which can be found in Table 3-2, is reduced from 151 μm to 71 μm when the GLR is increased from 4% to 8%. This is due to the liquid film being "squeezed" into a

thinner sheet from the increased gas flow rate. The equation that describes this liquid film thickness is given by Lin et al. [16] as follows:

$$d_L = d_0(1-\beta^{1/2})/2 \tag{3.1}$$

where d_0 is the nozzle orifice diameter and β is the flow-average void fraction given by Lin et al. [16] as:

$$\beta = Q_G/(Q_G + Q_L) \tag{3.2}$$

In this equation the variables Q_G and Q_L are the volumetric flow rates of the gas and liquid, respectively. If the SMD is normalized by this film thickness, which is controlled by the GLR, the values will be on the same order of magnitude as can be seen in Figure 3-3. In these figures the overall SMD distributions may be different, but it can be seen that the droplet size scales well with the film thickness. This shows that the droplet size is not controlled by the jet diameter but by the GLR which controls the film thickness.

The penetration height of the spray plume is also affected by different GLRs [16]. When comparing the two different GLRs in Figure 3-2, the 8% GLR condition often results in a height difference of 15 jet diameters. This results from the thinner liquid sheet exiting the injector at a higher velocity than the thicker liquid sheet at the lower GLR. A correlation for this height has been reported by Lin et al. [14]:

$$(h - h_0)/d_0 = 0.9(GLR)^{0.46} M^{-0.64} {q_0}^{0.34} (x/d_0)^{0.39} \tag{3.3}$$

where

$$h_0/d_0 = 3.17 {q_0}^{0.33} (x/d_0)^{0.40} \tag{3.4}$$

Here h is the penetration height, h_0 is the non-aerated penetration height, q_0 is the jet-to-freestream momentum ratio, and M is the freestream Mach number. The predicted penetration heights given by this correlation is listed in Table 3-1 and Table 3-2 with the measured values in the present study. The difference between the two is attributed to the fact that in Lin et al. [14] the penetration heights are taken using the 90% transmittance rule. The present measurements of h/d_0 listed in Table 3-1 and Table 3-2 are, however, the location of the highest droplets observed, so it is labeled as the maximum h/d_0.

Lin et al. [14] states that the GLR has little effect on the width of the spray plume. This also holds true in the current results. The correlation given for the width of the spray plume, w, is given as:

$$w/2d_0 = 3.07 {q_0}^{0.10} (x/d_0)^{0.45} \tag{3.5}$$

These predicted values are listed in Table 3-1 and Table 3-2 along with the present measurements. The present measurements are the maximum width of the spray so they are expected to be larger than the predicted value which defines the edge of the spray as the place where the volume flux is greater than 0.01 $cc/s/cm^2$.

3.3 Effect of Jet Exit Diameter

When the spray produced by the 1 mm injector is compared with the 0.5 mm injector the effects on the drop size are small. These effects can be seen in Figure 3-4, where each condition is compared side by side for the 1 mm and 0.5 mm injectors. The SMD distribution of the sprays remained relatively constant when only the jet exit diameter was changed. For the conditions in Figure 3-4, the overall SMD changed from 120 μm to 150 μm. This is most likely due to the fact that the droplet size is controlled more by the thickness of the liquid sheet exiting the injector which is controlled by the GLR, than the physical size of the jet diameter.

From Figure 3-4 it can be seen that the 0.5 mm injector did result in slightly higher jet penetration for the conditions in Figure 3-4, of $h/d_0 = 90$ (45 mm) compared to $h/d_0 = 60$ (60 mm) for the 1 mm injector even though the other conditions remained the same. However, this is more likely due to the non-dimensional scaling with the jet exit diameter than from any actual physical phenomenon. In addition to the larger penetration height produced by the smaller injector, the spray was also slightly wider for the same conditions with $w/2d_0 = 22$ for the small injector and $w/2d_0 = 19$ for the large injector. This is most likely due to the non-dimensional scaling with the smaller jet exit diameter. The most significant effect the jet diameter had on the spray was on the number of droplets that were produced. While the SMD distribution of the spray remained relatively constant the actual number of these droplets produced by the large injector was reduced by about one half the number of droplets for the small injector. This effect can be seen in the liquid volume fraction plots (Figure 3-5). The liquid volume fraction plots

show the concentration of droplets throughout the spray. This lower number of droplets is due to the fact that the flow rate of the liquid that was injected using the smaller injector (Q_L = 0.33 cc/s)) was lower than the flow rate of the liquid being injected into the larger injector (Q_L = 1.45 cc/s). This was done so that the q_0 would remain constant across the changing jet diameters.

3.4 Effect of Jet/Freestream Momentum Flux Ratio

The main effect of the jet/freestream momentum flux ratio was controlling the spray plume penetration, which agrees with the findings of Lin et al. [13-16]. The two jet/freestream momentum flux ratios investigated were q_0 = 0.74 and q_0 = 4. This effect can be seen in Figure 3-6. As expected the q_0 = 4 condition provided larger penetration heights than the q_0 = 0.74 condition.

The jet/freestream momentum flux ratio also has an effect on the spray plume width. As predicted by Eq. 3.3, as q_0 increases so does the spray plume width. It can be seen from Table 3-1 and Table 3-2 that at the higher values of q_0 the spray plume is wider than at similar conditions with a lower value of q_0.

3.5 Effect of Downstream Location

Any major change in droplet sizes as they travel downstream implies secondary breakup occurred between the two locations. It is expected that the droplet diameters should shrink some amount as they travel downstream due to evaporation, but large changes may indicate that something else is taking place, namely secondary breakup. The measured values of overall SMD are listed in Table 3-3. At the 8% GLR conditions

there is little or no change between the two downstream distances, but at the all of the 4% GLR conditions there is a considerable reduction in SMD of up to 60 μm. This could be evidence of secondary breakup in this region.

To determine if secondary breakup is occurring, the Weber number should be calculated in the questionable region. According to Hsiang and Faeth [31] drops will begin breaking up at We ≈ 10. The largest droplets for each condition will be considered since they are the best candidates for secondary breakup. Using these diameters the relative velocity between the air and the droplet needs to be calculated for each droplet. In order to do this the drag force needs to be considered to determine how much the droplet has accelerated due to the aerodynamic forces on the droplet. This must be done for both the x and y directions since the drag force will be in the direction of the droplet relative velocity; V_{rel}. The drop will be assumed to have an initial velocity equal to that of the jet exit velocity in the y direction upon breaking up from the jet exit [32]. These drop equation of motion relative the crossflow can be written as Eq. 3.6,

$$m\frac{d\vec{V}_{rel}}{dt} = -\frac{1}{2}\rho\left|V_{rel}\right|\vec{V}_{rel}C_d\pi\frac{d^2}{4} \tag{3.6}$$

where m is the mass of the droplet, ρ is the density of the freestream gas, C_d is the coefficient of drag on a sphere, and d is the droplet diameter. This equation can be written in the x- and y-directions and then be integrated to find the relative velocity components. The initial conditions (at t = 0) are as follows: $V_{rel,x} = -U_\infty$ and $V_{rel,y} = V_{jet}$ (V_{jet} is the exit velocity of the liquid from the injector calculated from the area of the liquid film and the liquid flow rate). This results in Eqs. 3.7 and 3.8.

$$V_{rel,x} = \frac{-8mU_\infty}{U_\infty \rho C_d \pi d^2 t + 8m} \tag{3.7}$$

$$V_{rel,y} = \frac{8mV_j}{V_j \rho C_d \pi d^2 t + 8m} \tag{3.8}$$

The x-component of the drop absolute velocity can be integrated in order to determine the time it takes each droplet to travel to the downstream location in question. Applying the boundary condition of x = 0 at t = 0 results in Eq. 3.9.

$$x = \frac{8m}{\rho C_d \pi d^2} \ln\left[\frac{8m}{U_\infty \rho C_d \pi d^2 t + 8m}\right] + U_\infty t \tag{3.9}$$

Using this equation and different downstream distances, droplet diameters, and the other test conditions, the times it takes larger droplets to reach the planes of measurement can be found. These times can then be used to determine the velocity in the x direction and the times from Eq. 3.7 can be used to determine the velocity in the y direction. These components can be used to determine the magnitude of the relative velocities, and using these velocities the Weber number can be calculated. This results in Weber numbers that are on the order of 10. This means that secondary breakup is likely occurring in this area, which in turn explains the large reductions in SMD found in Table 3-3. However, these velocities need to be experimentally validated to support these theoretical results.

Other properties such as spray plume penetration and spray plume width are also being affected by downstream distance. It is evident the spray is continuing to increase in height and width as it travels from $x/d_0 = 25$ to $x/d_0 = 50$. This means that the droplets are still retaining their initial momentum and did not relax to the local conditions.

3.6 Overall Droplet Distribution

According to Simmons [33] if the drop sizes are normalized by their mass median diameter (MMD) and plotted on a root-normal scale, the drop size distribution of all injectors should fall on a line where the MMD/SMD = 1.2. Figure 3-7 shows the present study's data on this type of plot. It can be seen that the majority of these points do fall on this line. However, some of the test conditions do not follow this trend. At the conditions of 4% GLR the values fall below this line. This is due to the fact that there are more large droplets at the 4% GLR condition which shifts the MMD toward the SMD.

d_0 (mm)	0.5	0.5	0.5	0.5	0.5	0.5	0.5	0.5
M (-)	0.16	0.16	0.16	0.16	0.07	0.07	0.07	0.07
x/d_0 (-)	25	50	25	50	25	50	25	50
q_0 (-)	0.74	0.74	0.74	0.74	4	4	4	4
GLR (%)	4	4	8	8	4	4	8	8
$Q_{L,injected}$ (cc/s)	0.33	0.33	0.33	0.33	0.33	0.33	0.33	0.33
$Q_{G,injected}$ (cc/s)	10.8	10.8	21.7	21.7	10.8	10.8	21.7	21.7
SMD (μm)	154	97	75	62	168	149	74	70
h / d_0 from Lin et al [14](-)	38	50	45	59	89	117	109	143
Present measurement h / d_0 (-)	60	90	60	90	120	180	120	180
w / $2d_0$ from Lin et al [14](-)	12.7	17.3	12.7	17.3	15	20.5	15	20.5
Present measurement w / $2d_0$ (-)	22	22	17	22	22	30	24	28

Table 3-1 Summary of results for 0.5 mm injector

d_0 (mm)	1.0	1.0	1.0	1.0	1.0	1.0	1.0	1.0
M (-)	0.18	0.18	0.18	0.18	0.075	0.075	0.075	0.075
x/d_0 (-)	25	50	25	50	25	50	25	50
q_0 (-)	0.74	0.74	0.74	0.74	4	4	4	4
GLR (%)	4	4	8	8	4	4	8	8
$Q_{L,injected}$ (cc/s)	1.45	1.45	1.45	1.45	1.45	1.45	1.45	1.45
$Q_{G,injected}$ (cc/s)	49	49	103	103	49	49	103	103
SMD (μm)	151	118	72	59	164	106	86	73
h / d_0 from Lin et al [14](-)	27	35	33	43	68	90	87	115
Present measurement h / d_0 (-)	45	60	60	75	105	120	90	120
w / $2d_0$ from Lin et al [14](-)	12.7	17.3	12.7	17.3	15	20.5	15	20.5
Present measurement w / $2d_0$ (-)	12.5	18.5	14.5	21	19.5	25	21.5	25.5

Table 3-2 Summary of results for 1.0 mm injector

d_0 (mm)	GLR	q_0	v_∞ (m/s)	d_L (μm)	v_{jet} (m/s)	x/d	D_{max} (μm)	Overall SMD (μm)	% Reduction
1	4%	0.74	61	7.2	64	25	351	151	
1	4%	0.74	61	7.2	64	50	274	118	22%
1	4%	4	26	7.2	64	25	337	164	
1	4%	4	26	7.2	64	50	239	106	35%
0.5	4%	0.74	56	3.7	56	25	157	154	
0.5	4%	0.74	56	3.7	56	50	113	97	37%
0.5	4%	4	24.2	3.7	56	25	183	168	
0.5	4%	4	24.2	3.7	56	50	171	149	11%
1	8%	0.74	61	3.5	133	25	257	72	
1	8%	0.74	61	3.5	133	50	184	59	18%
1	8%	4	26	3.5	133	25	407	86	
1	8%	4	26	3.5	133	50	294	73	15%
0.5	8%	0.74	56	1.9	112	25	147	75	
0.5	8%	0.74	56	1.9	112	50	157	62	17%
0.5	8%	4	24.2	1.9	112	25	140	74	
0.5	8%	4	24.2	1.9	112	50	167	70	5%

Table 3-3 SMD reduction at x/d = 25 and 50 for each of the test conditions

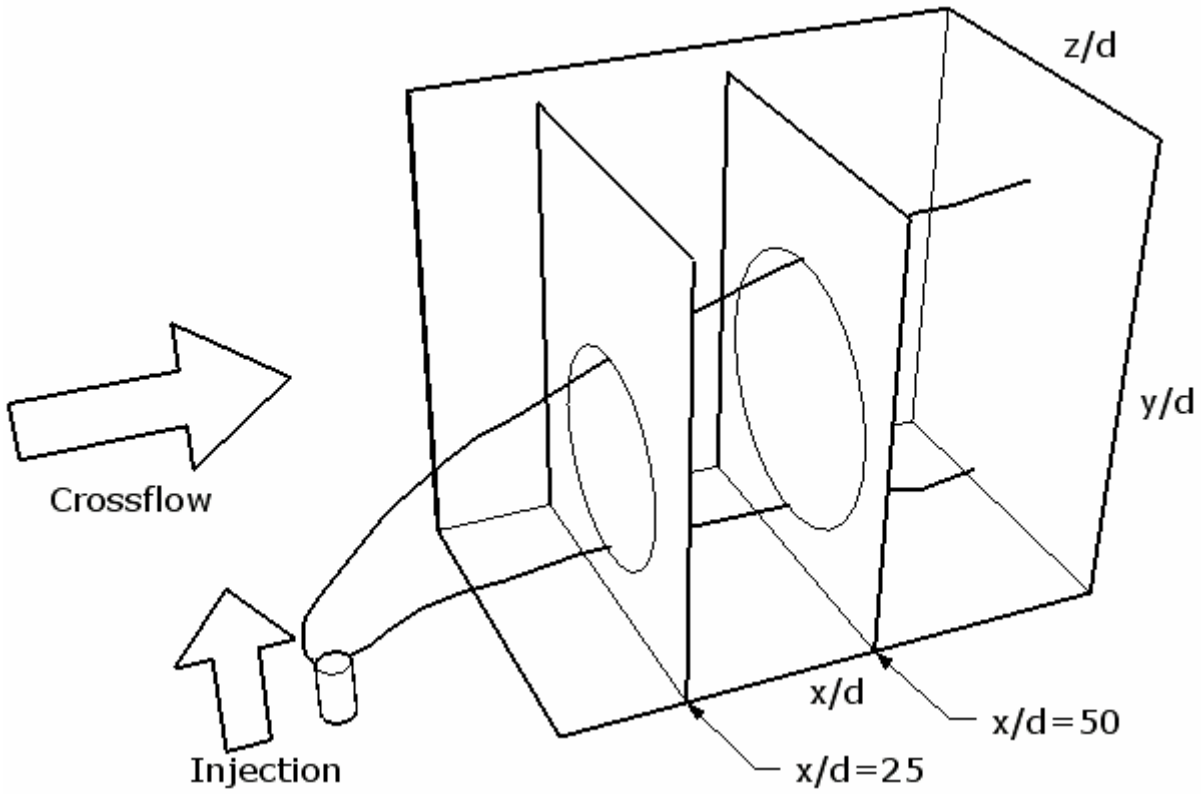

Figure 3-1 Sketch showing the orientation of Figures 3-2 through 3-6.

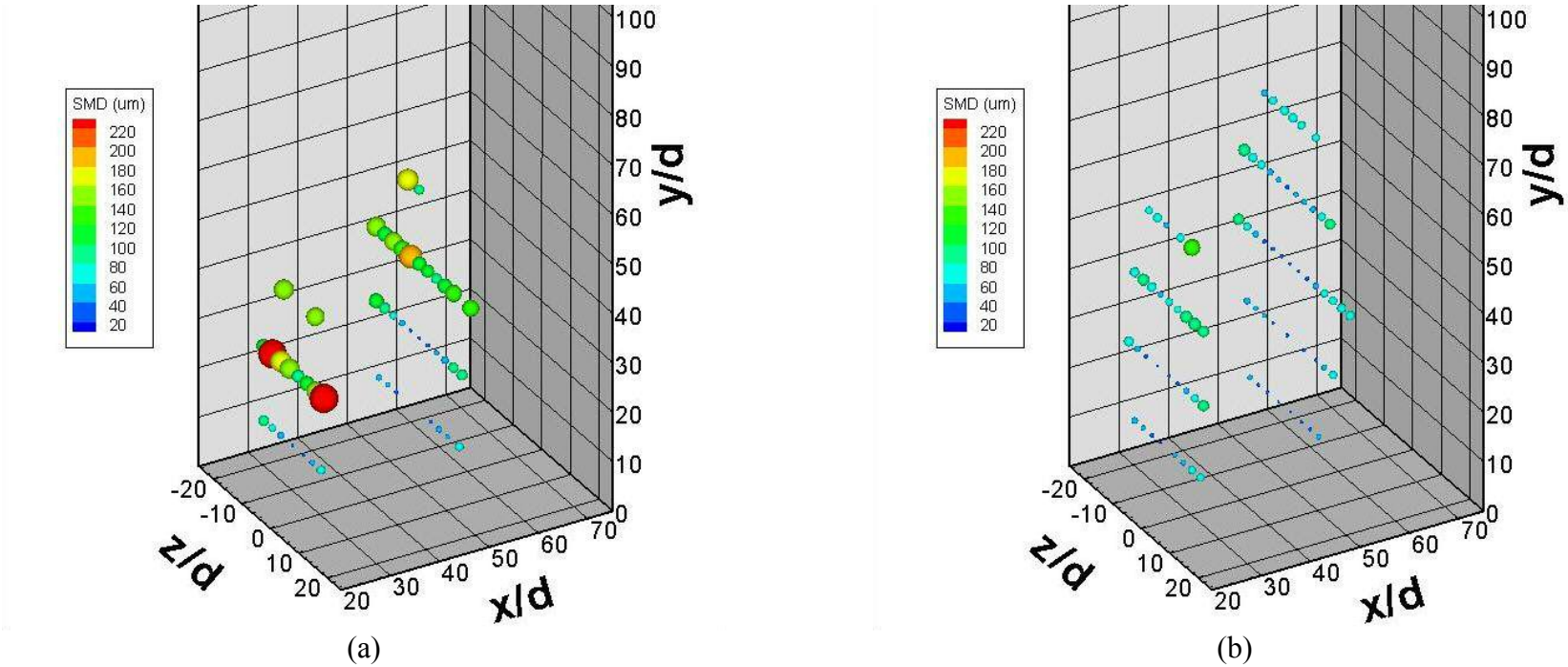

Figure 3-2 Effect of GLR: (a) SMD Distribution at GLR=4%, q_0=0.74, and d_0=1 mm and (b) SMD Distribution at GLR=8%, q_0=0.74, and d_0=1 mm

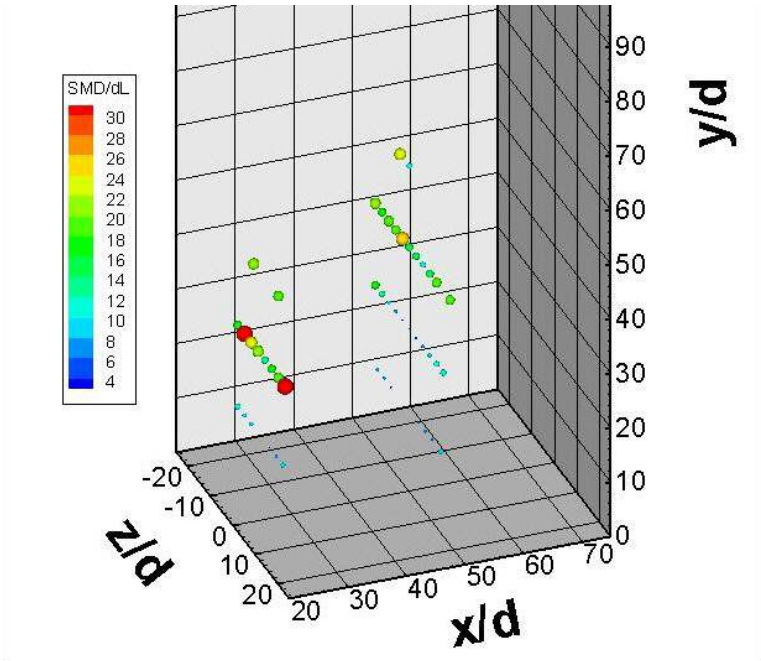

(a)

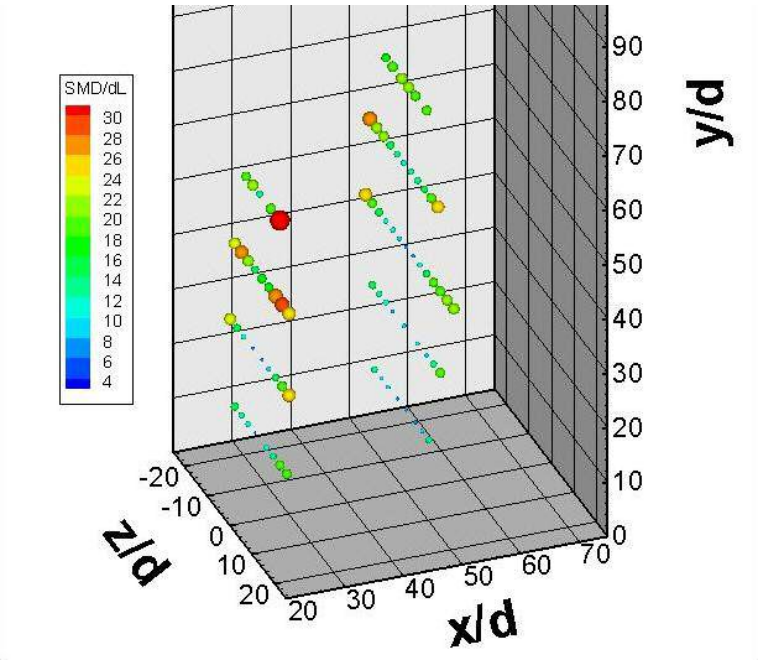

(b)

Figure 3-3 SMD Normalized by Film Thickness at: (a) GLR=4%, q_0=0.74, and d_0=1 mm and (b) GLR=8%, q_0=0.74, and d_0=1 mm

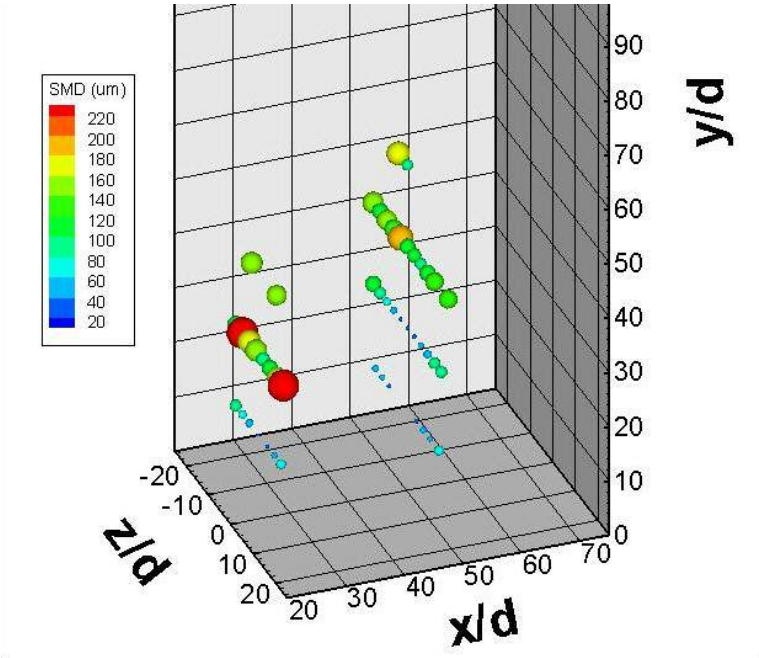

(a)

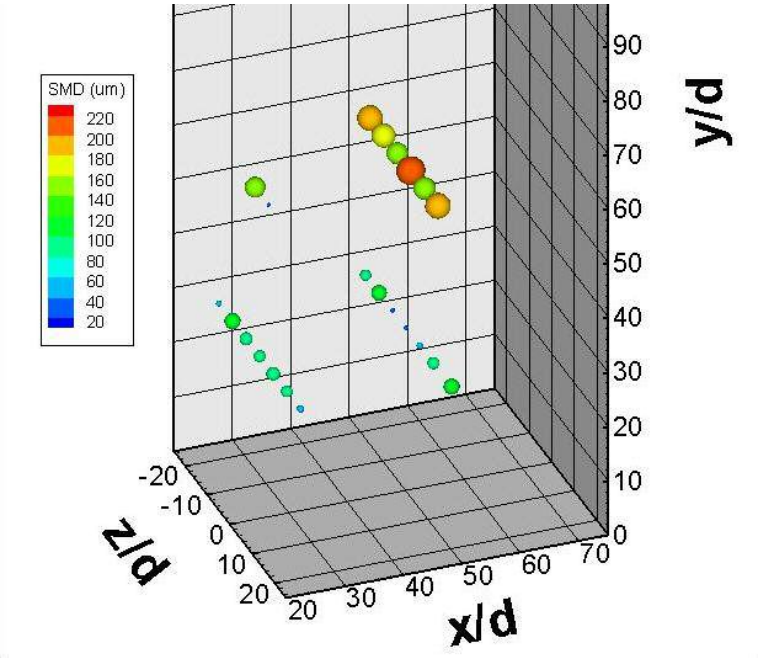

(b)

Figure 3-4 Effect of jet diameter: (a) SMD Distribution at GLR=4%, q_0=0.74, and d_0=1 mm and SMD Distribution at GLR=4%, q_0=0.74, and d_0=0.5 mm

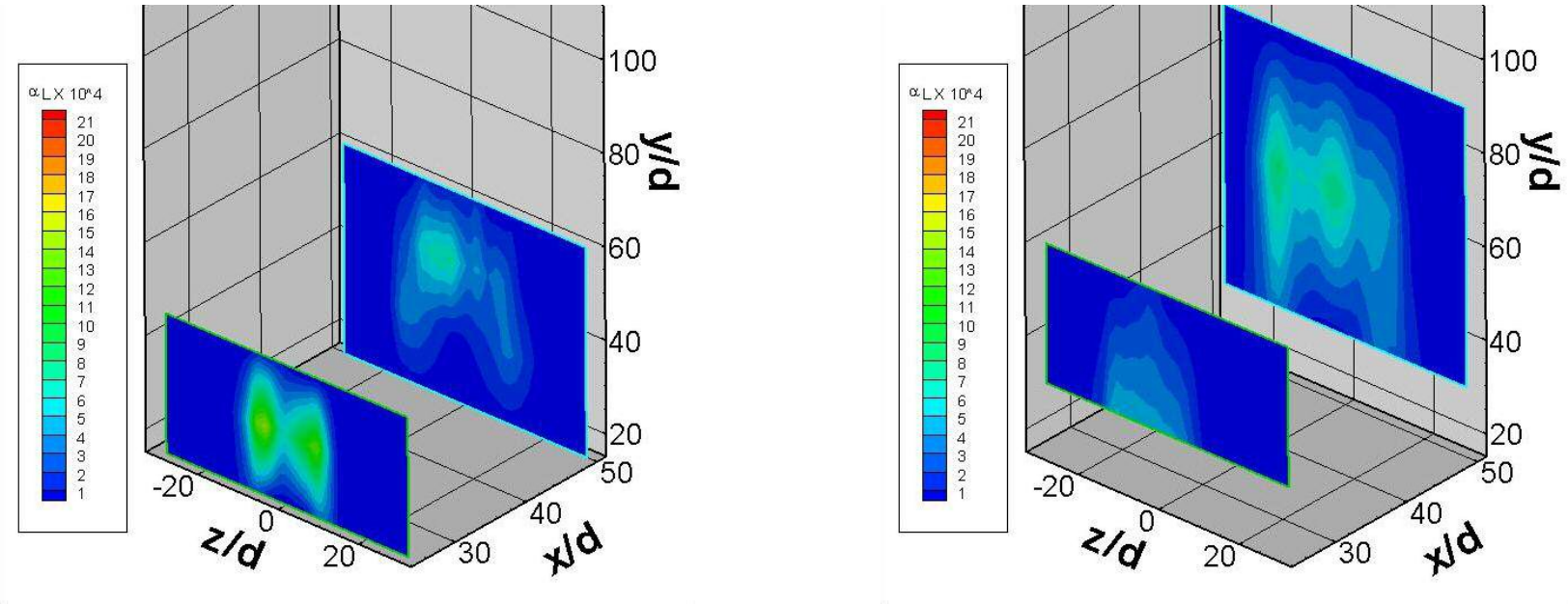

(a)

(b)

Figure 3-5 Volume fraction plot at (a) GLR=4%, q_0=0.74, and d_0=1 mm and (b) GLR=4%, q_0=0.74, and d_0=0.5 mm

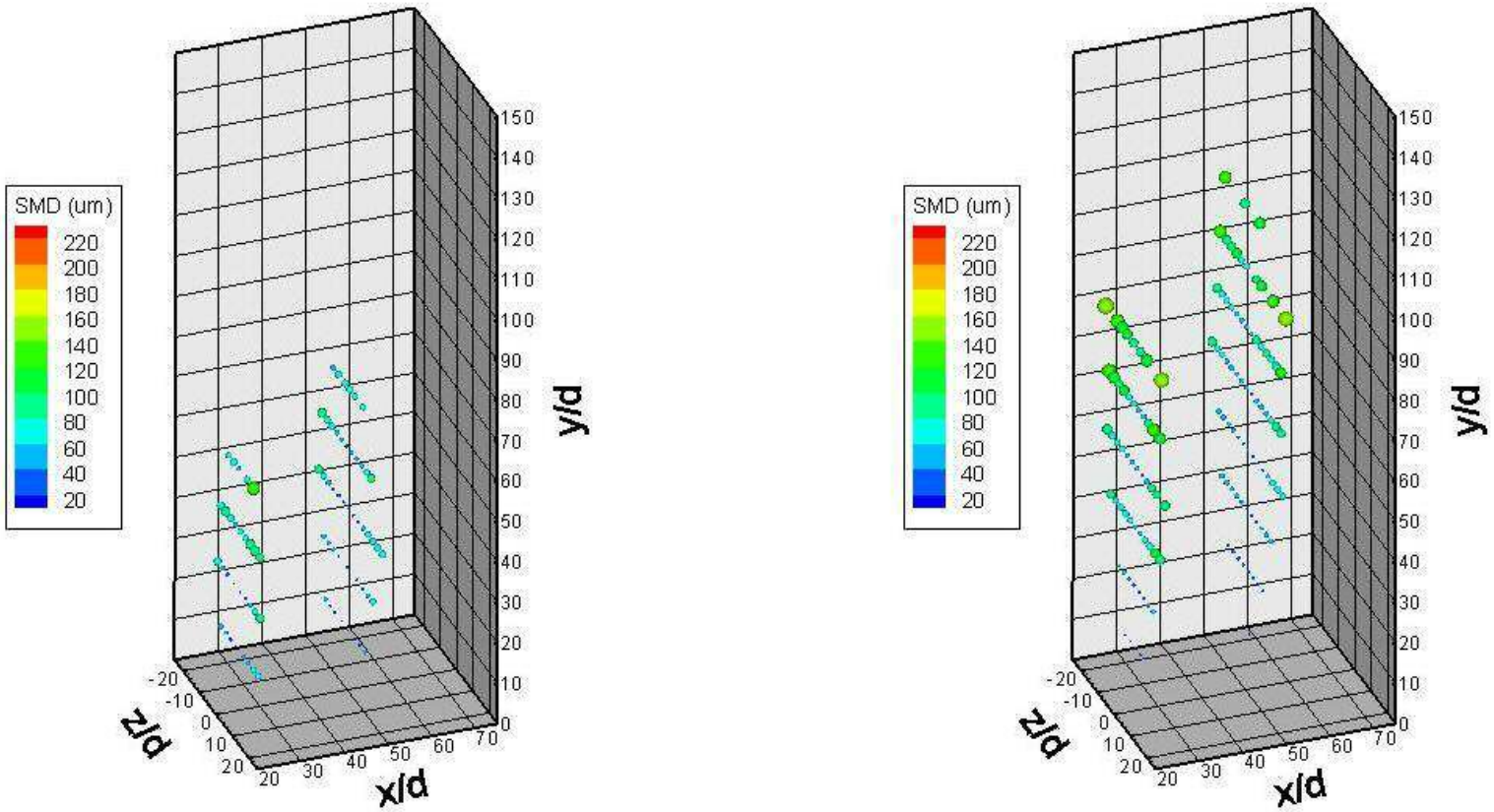

Figure 3-6 Effect of q_0: (a) SMD Distribution at GLR=8%, q_0=0.74, and d_0=1 mm and (b) SMD Distribution at GLR=8%, q_0=4, and d_0=1 mm

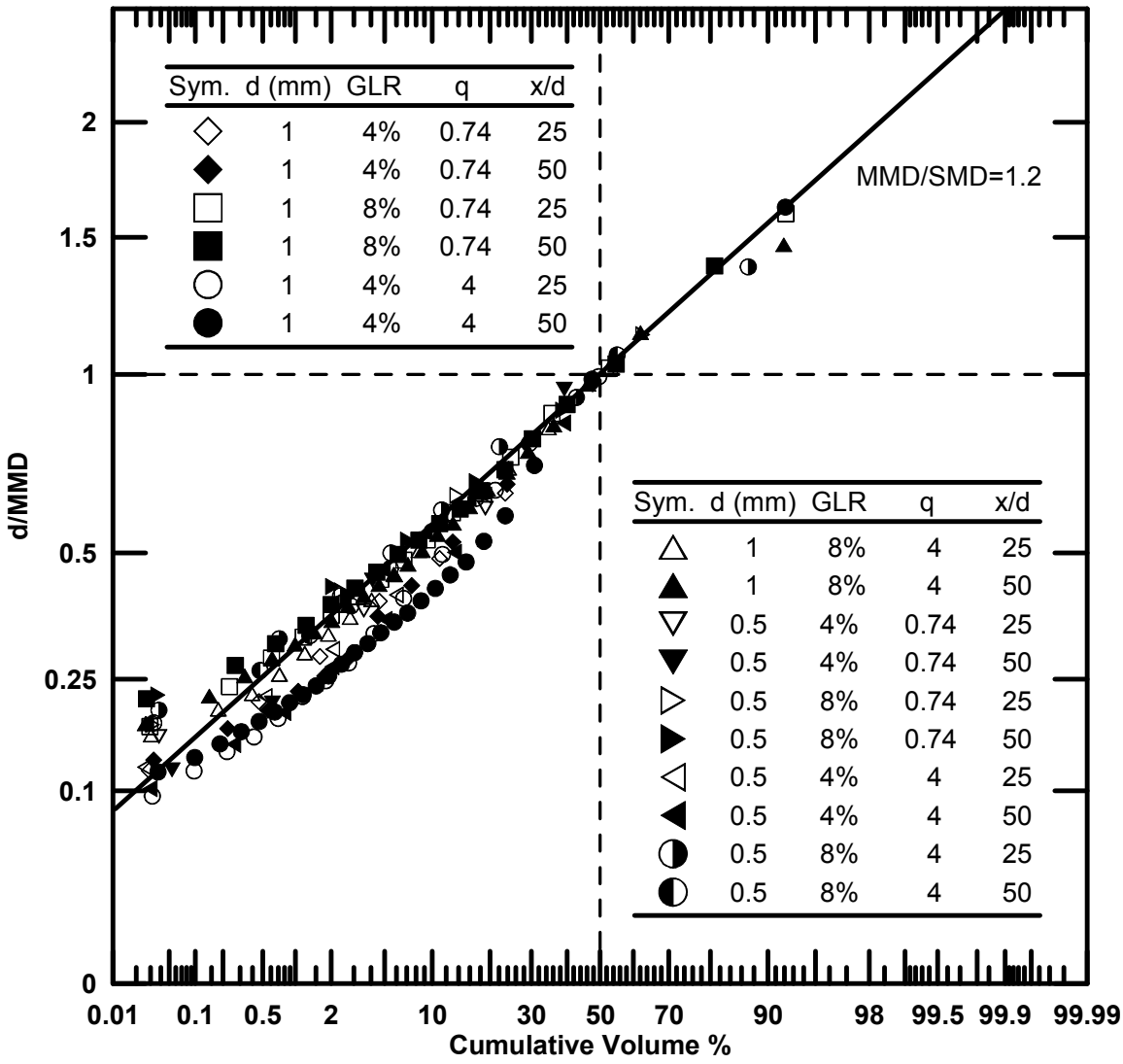

Figure 3-7 Droplet size distribution plot.

Chapter 4.

Summary and Conclusions

4.1 Summary

The spray produced by an aerated-liquid injector in a subsonic crossflow was investigated using digital holography. Two methods of holography were tested: digital in-line holography and digital holographic microscopy. The latter method provided the best results with the ability to resolve the smaller droplets in the spray. Using the holographic methods the spray volume was analyzed at the conditions of: 1 mm and 0.5 mm injector exit diameters, 4% and 8% GLR, 25 and 50 jet diameters downstream, and jet-to-freestream momentum ratios of 0.74 and 4. SMD distribution maps were made at each of the conditions, and from these distributions the effects of each variable could be seen.

4.2 Conclusions

This work has managed to probe the aerated injectors in the optically challenging near injector area. The present study found evidence of secondary breakup in some of the test conditions. The major conclusions are as follows:

1. Digital holography is a useful tool for examining this dense near injector area and can provide information other methods can not. This is due to the fact that it is

insensitive to non-spherical droplets, and that it can work well in the near injector area.

2. Digital holographic microscopy works better than the standard digital in-line holography. It removes a substantial amount of noise because of the elimination of the additional lenses needed with the in-line method.
3. As the GLR increased from 4% to 8% droplet sizes decreased. The droplet sizes were independent of other variables such as injector diameter and jet-to-freestream momentum flux ratio had little effect on droplet size. Drop sizes were found to correlate with the film thickness which is a function of the GLR.
4. Reductions in droplet sizes at the GLR = 4% conditions between the two downstream locations of x/d=25 and x/d = 50 showed signs of secondary breakup. Upon further investigation of the theoretical Weber numbers it is clear that secondary breakup is likely occurring between the two downstream locations.

4.3 Recommendations for Future Studies

1. The process of measuring the droplets needs to be automated. Currently, the measurement process is done manually and is very time consuming. With the knowledge of how to find the plane of focus automatically this automation is a reasonable idea.
2. The digital holographic microscopy method worked well at the x/d_0=25 location and should be applied even closer to the injector. There were no limitations at this location and by using this method more information can be obtained even

closer to the injector exit. This will give a better idea of where secondary breakup processes are occurring.

3. The addition of double pulsed holograms would add valuable droplet velocity information. The velocity measurements could also be automated using the same principles used in PIV. By recording the location of the centroids of droplets in two frames separated by a short time, the velocity measurements could be made using the statistical methods of PIV. By automating the diameter measurements and velocity measurements the technique used in this study would have a wide range of applications to many sprays and particle fields.
4. By automating the diameter measurements and velocity measurements the technique used in this study would have a wide range of applications to many sprays and particle fields. This additional information would give a clearer picture of what is actually happening within this complex spray.

References

1 Yua, G., Lia, J.G., Zhaoa, J.R., Yuea, L.J., Changa, X.Y. and Sung, C.-J. An experimental study of kerosene combustion in a supersonic model combustor using effervescent atomization. *Proceeding of the Combustion Institute*, 2005, 30, 2859-2866.

2 Sovani, S.D., Sojka, P.E. and Lefebvre, A.H. Effervescent Atomization. *Progress in Energy and Combustion Science*, 2001, 27, 483-521.

3 Lefebvre, A.H., Wang, X.F. and Martin, C.A. Spray Characteristics of Aerated-Liquid Pressure Atomizers. *Journal of Propulsion*, 1988, 4(4), 293-298.

4 Chin, J.S. and Lefebvre, A.H. A Design Procedure for Effervescent Atomizers. *Journal of Engineering for Gas Turbines and Power - Transactions of the ASME*, 1995, 117(2), 266-271.

5 Kim, J.Y. and Lee, S.Y. Dependence of Spraying Performance on the Internal Flow Pattern in Effervescent Atomizers. *Atomization and Sprays*, 2001, 11, 735-756.

6 Lin, K.-C., Kennedy, P.J. and Jackson, T.A. Structures of Internal Flow and the Corresponding Spray for Aerated-Liquid Injectors. *37th AIAA/ASME/SAE/ASEE Joint Propulsion Conference*, pp. 1-10Salt Lake City, Utah, 2001).

7 Santangelo, P.J. and Sojka, P.E. A Holographic Investigation of an Effervescent Atomizer-Produced Spray. *Atomization and Sprays*, 1995, 5, 137-155.

8 Wade, R.A., Weerts, J.M., Sojka, P.E., Gore, J.P. and Eckerle, W.A. Effervescent atomization at injection pressures in the MPa range *Atomization and Sprays*, 1999, 9(6), 651-657.

9 Sovani, S.D., Chou, E., Sojka, P.E., Gore, J.P., Eckerle, W.A. and Crofts, J.D. High pressure effervescent atomization: effect of ambient pressure on spray cone angle. *Fuel*, 2001, 80, 427-435.

10 Chen, S.K., Lefebvre, A.H. and Rollbuhler, J. Influence of Ambient Air Pressure on Effervescent Atomization. *Journal of Propulsion and Power*, 1993, 9(1), 10-15.

11 Buckner, H.N. and Sojka, P.E. Effervescent Atomization of High-Viscosity Fluids: Part I. Newtonian Liquids. *Atomization and Sprays*, 1991, 1, 239-252.

12 Lund, M.T., Sojka, P.E., Lefebvre, A.H. and Gosselin, P.G. Effervescent atomization at low mass Fow rates Part 1: the infuence of surface tension. *Atomization and Sprays*, 1993, 3, 77-89.

13 Lin, K.-C., Kennedy, P.J. and Jackson, T.A. Penetration Heights of Liquid Jets in High-Speed Crossflows. *40th AIAA Aerospace Sciences Meeting and Exhibit*Reno, Nevada, 2002).

14 Lin, K.-C., Kennedy, P.J. and Jackson, T.A. Structures of Aerated Liquid Jets in High Speed Crossflows. *32nd AIAA Fluid Dynamics Conference*, pp. 1-12St. Louis, Missouri, 2002).

15 Lin, K.-C., Kennedy, P.J. and Jackson, T.A. Spray Structures of Aerated-Liquid Jets in Subsonic Crossflows. *32nd AIAA Aerospace Sciences Meeting*, pp. 1-18Reno, Nevada, 2001).

16 Lin, K.-C., Kirkendall, K.A., Kennedy, P.J. and Jackson, T.A. Spray Structures of Aerated Liquid Fuel Jets in Supersonic Crossflows. *35th AIAA/ASME/SAE/ASEE Joint Propusion Conference and Exhibit*, pp. 1-11Los Angeles, California, 1999).

17 Sutherland, J.J., Sojka, P.E. and Plesniak, M.W. Ligament controlled effervescent atomization. *Atomization and Sprays*, 1997, 7(4), 383-406.

18 Gabor, D. A New Microscopic Principle. *Nature*, 1948, 161(4098), 777-778.

19 Goodman, J.W. and Lawrence, R.W. Digital Image Formation from Electronically Detected Holograms. *Applied Physics Letters*, 1967, 11(3), 77-79.

20 Schnars, U. and Juptner, W. Direct Recording of Holograms by a CCD Target and Numerical Reconstruction. *Applied Optics*, 1994, 33(2), 179-181.

21 Jones, A.R., Sarjeant, M., Davis, C.R. and Denham, R. Application of in-line holography to drop size measurement in dense fuel sprays. *Applied Optics*, 1977, 17(3), 328-333.

22 Meng, H., Anderson, W.L., Hussain, F. and Liu, D.D. Intrinsic speckle noise in in-line particle holography. *Journal of the Optical Society of America A*, 1993, 10(9), 2046-2058.

23 Schnars, U. and Jueptner, W. *Digital Holography: Digital Hologram Recording, Numerical Reconstruction, and Related Techniques*. (Springer, Berlin, 2005).

24 Meng, H. and Hussain, F. In-line recording and off-axis viewing technique for holographic particle velocimetry. *Applied Optics*, 1995, 34(11), 1827-1840.

25 Kreis, T.M., Adams, M. and Jüptner, W.P. Methods of Digital Holography: A Comparison. *SPIE*, 1997, 3098, 224-233.

26 Sallam, K., Aalburg, C., Faeth, G.M., Lin, K.-C., Carter, C.D. and Jackson, T.A. Primary Breakup of Round Aerated-Liquid Jets in Supersonic Crossflows. *Atomization and Sprays*, 2006, 16, 657-672.

27 Bar-Kohany, T. and Sher, E. Subsonic Effervescent Atomization: A Theoretical Approach. *Atomization and Sprays*, 2004, 14, 495-509.

28 Lorcher, M., Schmidt, F. and Mewes, D. Effervescent Atomization of Liquids. *Atomization and Sprays*, 2005, 15, 145-168.

29 Petersen, F.J., Wørts, O., Schæfer, T. and Sojka, P.E. Design and Atomization Properties for an Inside-Out Type Effervescent Atomizer. *Drug Deverlopment and industrial Pharmacy*, 2004, 30(3), 319-326.

30 Sovani, S.D., Crofts, J.D., Sojka, P.E., Gore, J.P. and Eckerle, W.A. Structure and steady-state spray performance of an effervescent diesel injector. *Fuel*, 2005, 84, 1503-1514.

31 Hsiang, L.-P. and Faeth, G.M. Drop Deformation and Breakup due to Shock Wave and Steady Disturbances. *International Journal of Multiphase Flow*, 1995, 21(4), 545-560.

32 Sallam, K.A., Aalburg, C. and Faeth, G.M. Breakup of Round Liquid Jets in Gaseous Crossflow. *AIAA*, 2004, 42(12), 2529-2540.

33 Simmons, H.C. The Correlation of Drop-Size Distributions in Fuel Nozzle Sprays. *Journal of Engineering for Power*, 1977, 99(3), 309-319.

Appendix A

SMD and Liquid Volume Fraction Distributions

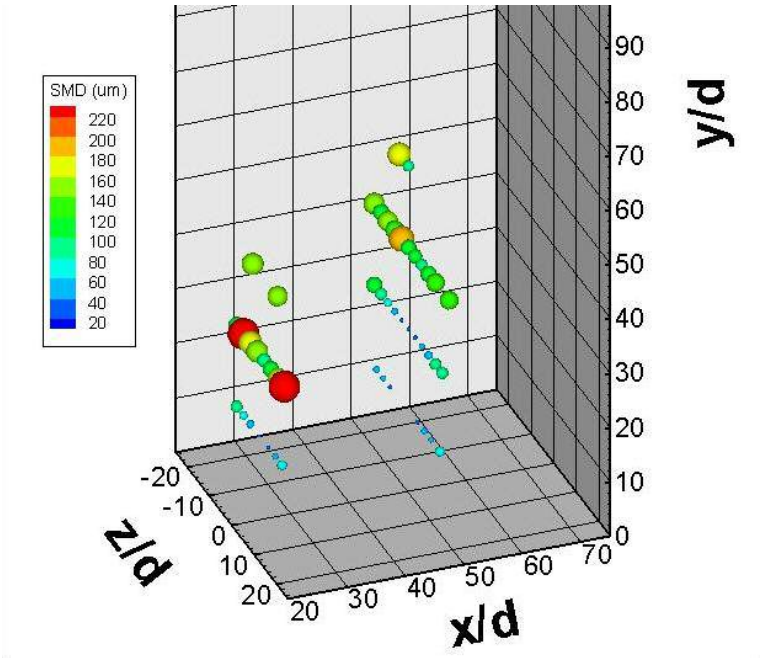

Figure A-4-1 SMD Distribution at GLR=4%, q_0=0.74, and d_0=1 mm

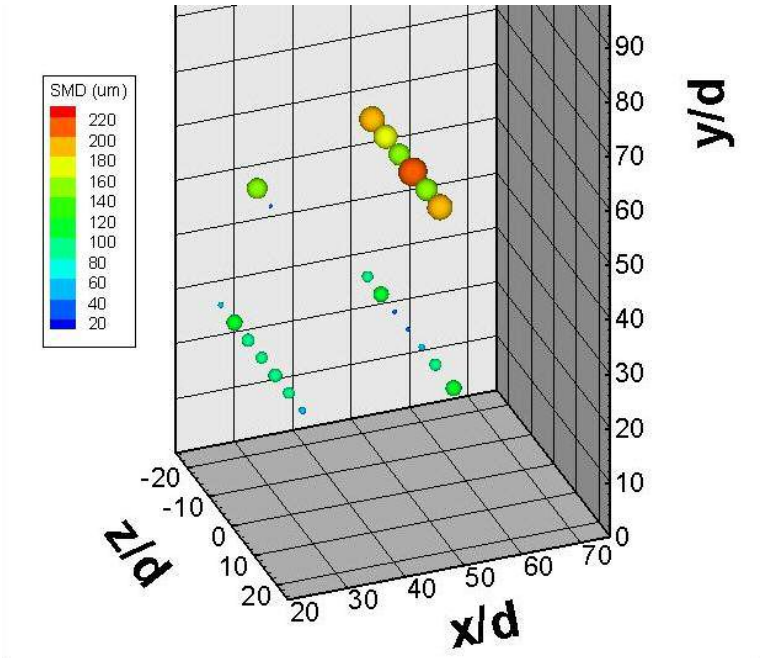

Figure A-4-2 SMD Distribution at GLR=4%, q_0=0.74, and d_0=0.5 mm

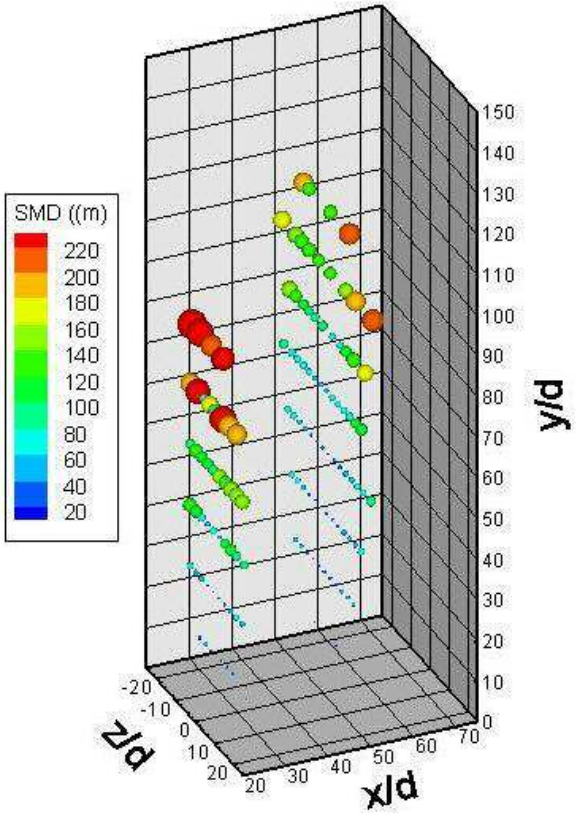

Figure A-4-3 SMD Distribution at GLR=4%, q_0=4, and d_0=1 mm

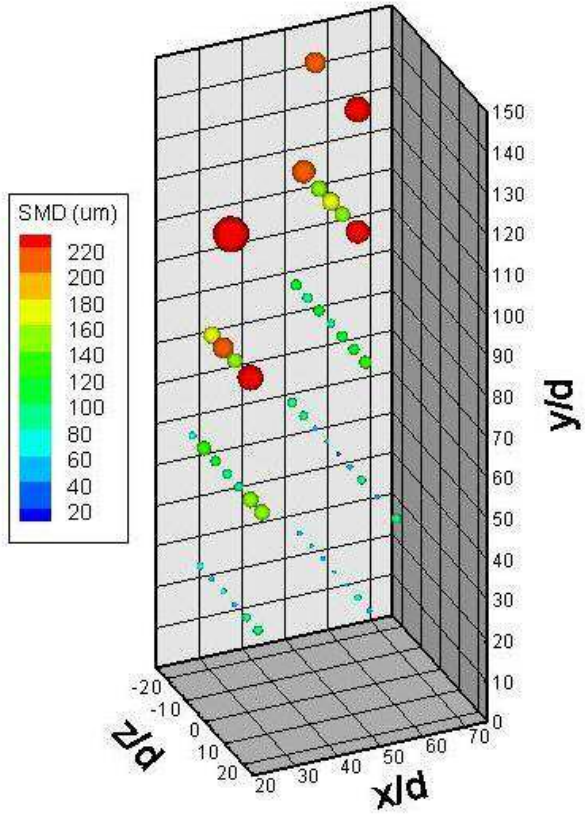

Figure A-4-4 SMD Distribution at GLR=4%, q_0=4, and d_0=0.5 mm

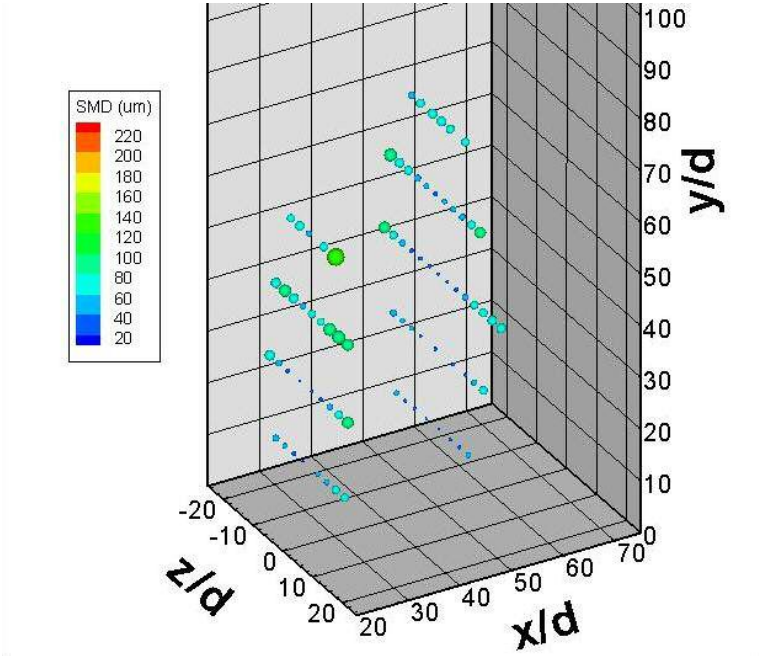

Figure A-4-5 SMD Distribution at GLR=8%, q_0=0.74, and d_0=1 mm

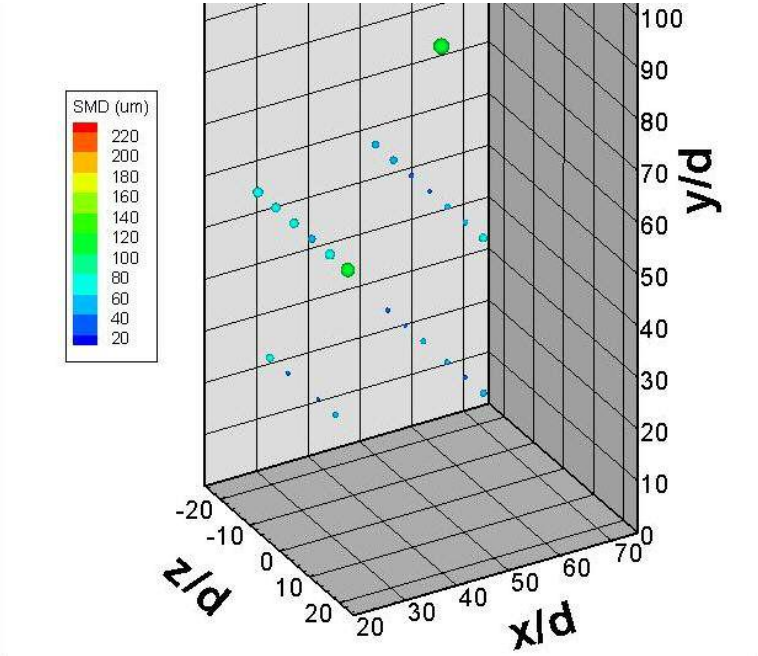

Figure A-4-6 SMD Distribution at GLR=8%, q_0=0.74, and d_0=0.5 mm

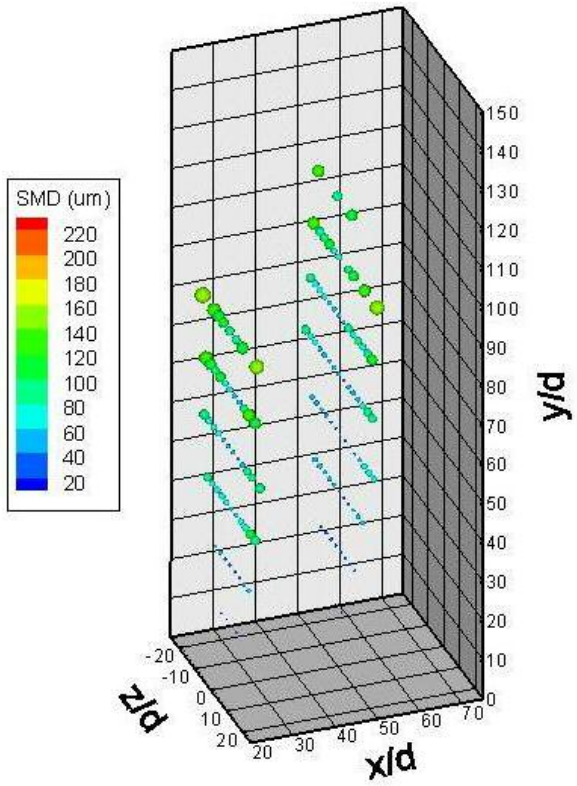

Figure A-4-7 SMD Distribution at GLR=8%, q_0=4, and d_0=1 mm

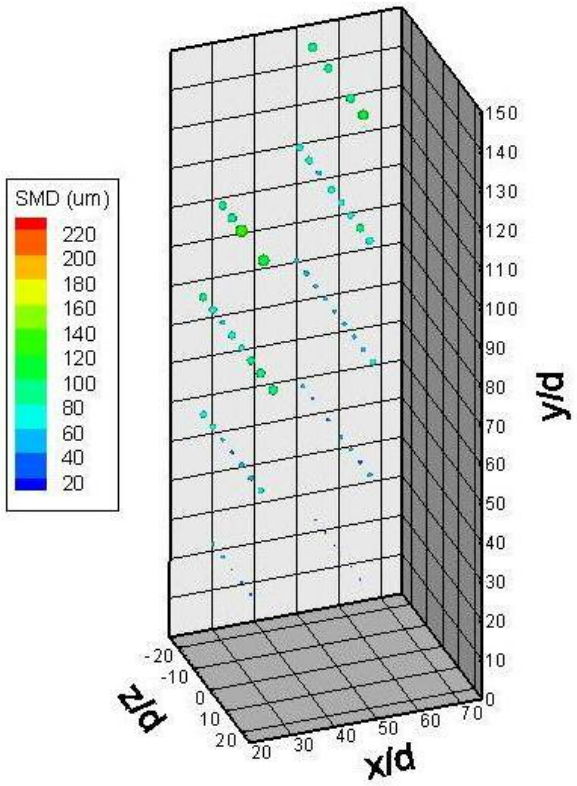

Figure A-4-8 SMD Distribution at GLR=8%, q_0=4, and d_0=0.5 mm

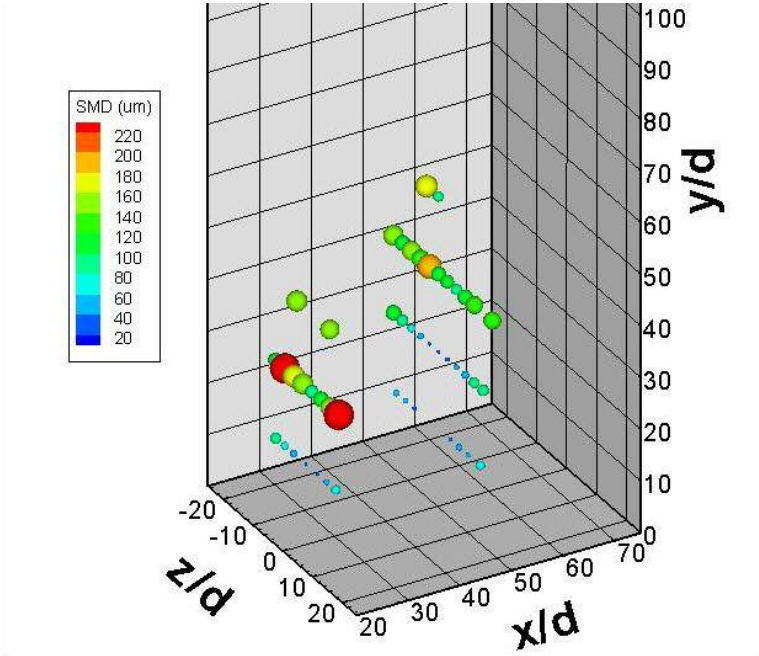

Figure A-4-9 SMD Distribution at GLR=4%, q_0=0.74, and d_0=1 mm

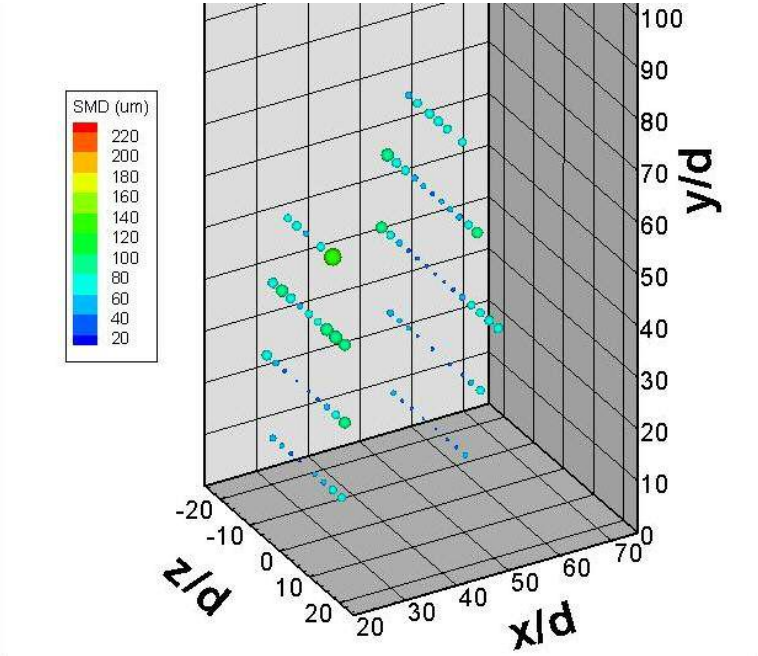

Figure A-4-10 SMD Distribution at GLR=8%, q_0=0.74, and d_0=1 mm

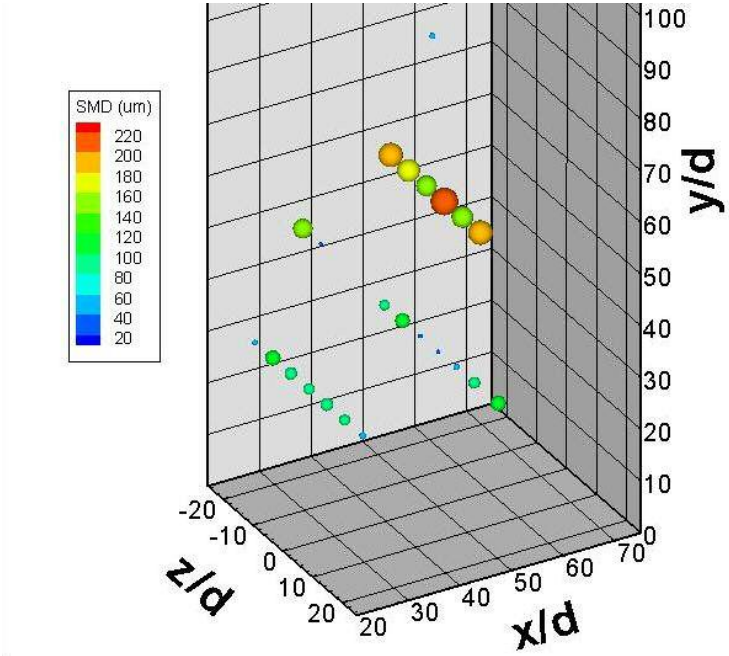

Figure A-4-11 SMD Distribution at GLR=4%, q_0=0.74, and d_0=0.5 mm

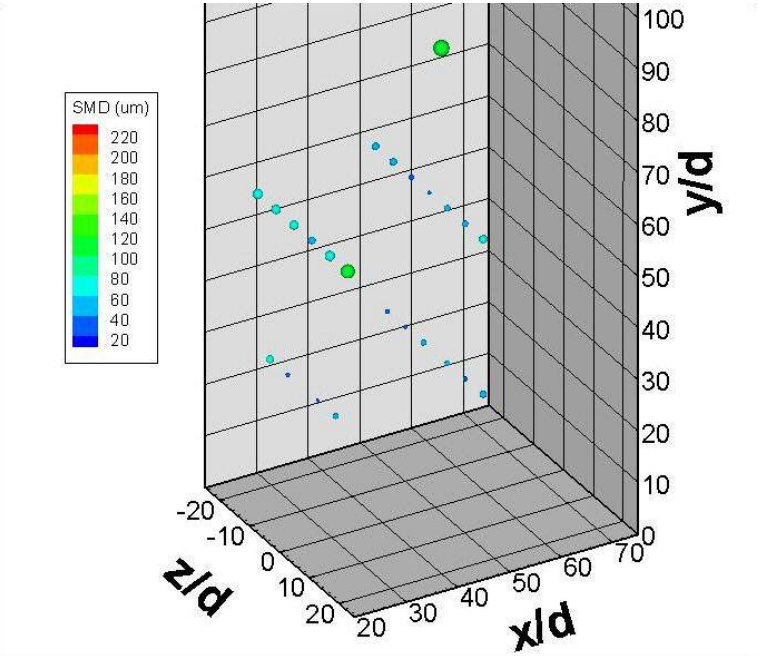

Figure A-4-12 SMD Distribution at GLR=8%, q_0=0.74, and d_0=0.5 mm

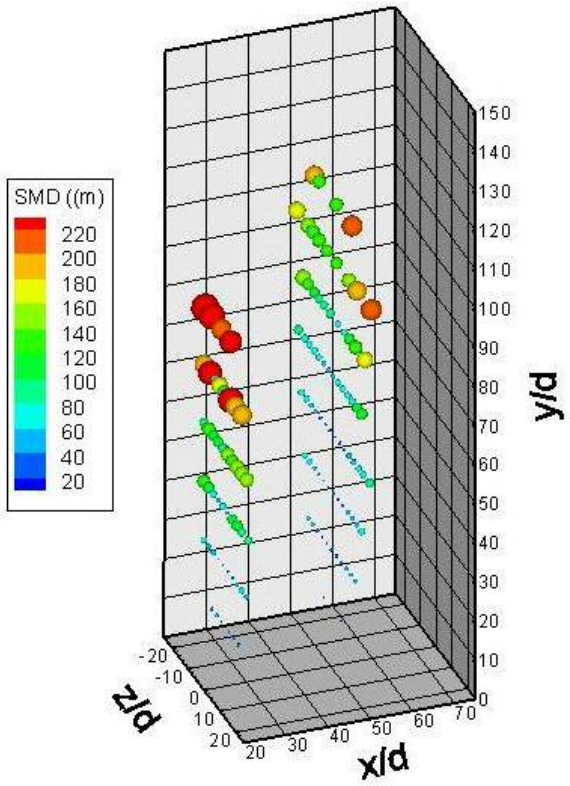

Figure A-4-13 SMD Distribution at GLR=4%, q_0=4, and d_0=1 mm

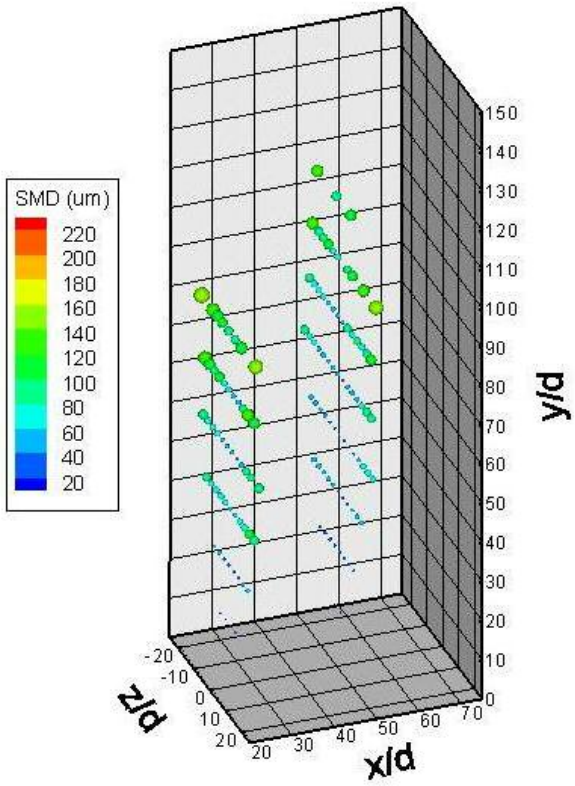

Figure A-4-14 SMD Distribution at GLR=8%, q_0=4, and d_0=1 mm

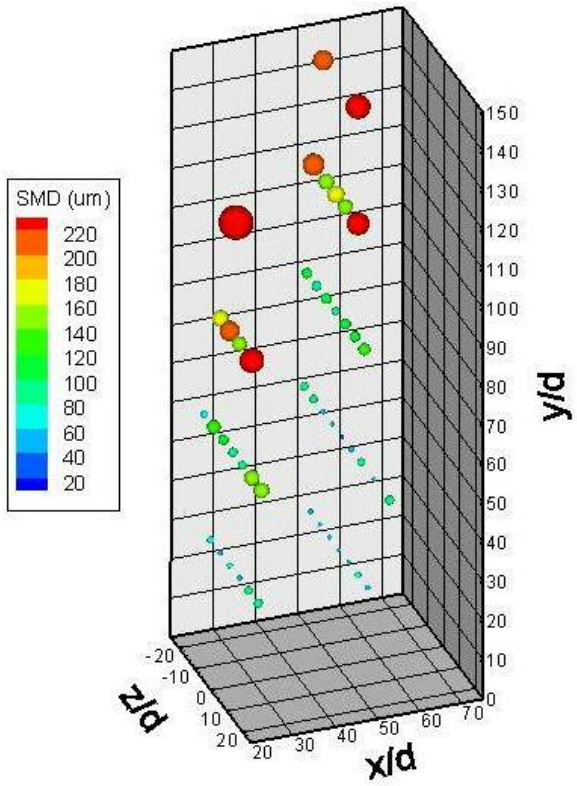

Figure A-4-15 SMD Distribution at GLR=4%, q_0=4, and d_0=0.5 mm

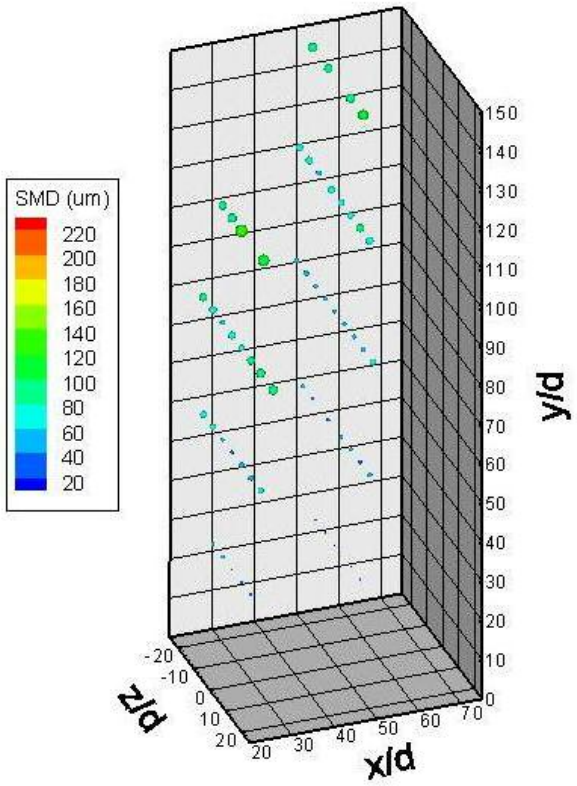

Figure A-4-16 SMD Distribution at GLR=8%, q_0=4, and d_0=0.5 mm

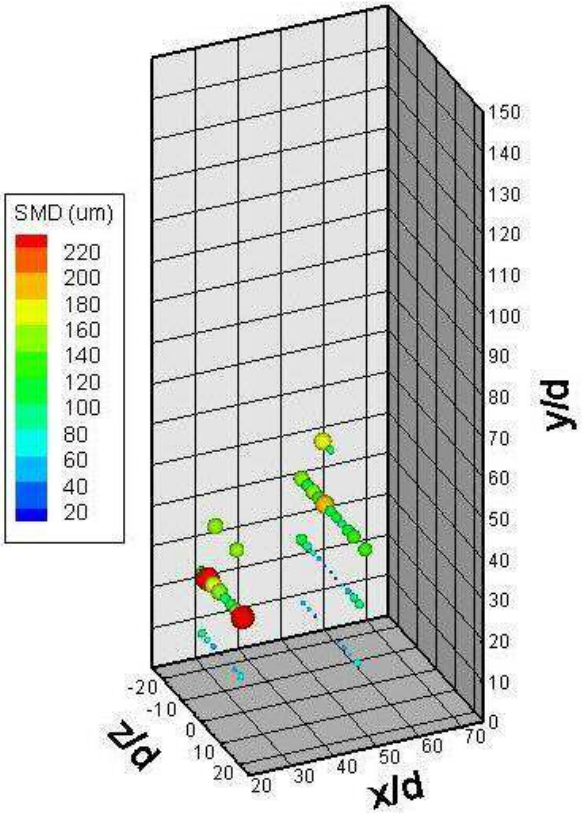

Figure A-4-17 SMD Distribution at GLR=4%, q_0=0.74, and d_0=1 mm

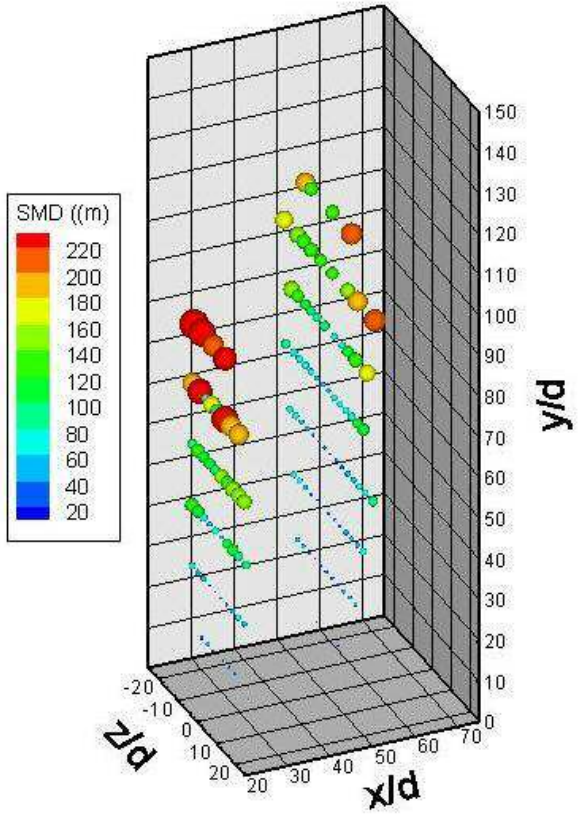

Figure A-4-18 SMD Distribution at GLR=4%, q_0=4, and d_0=1 mm

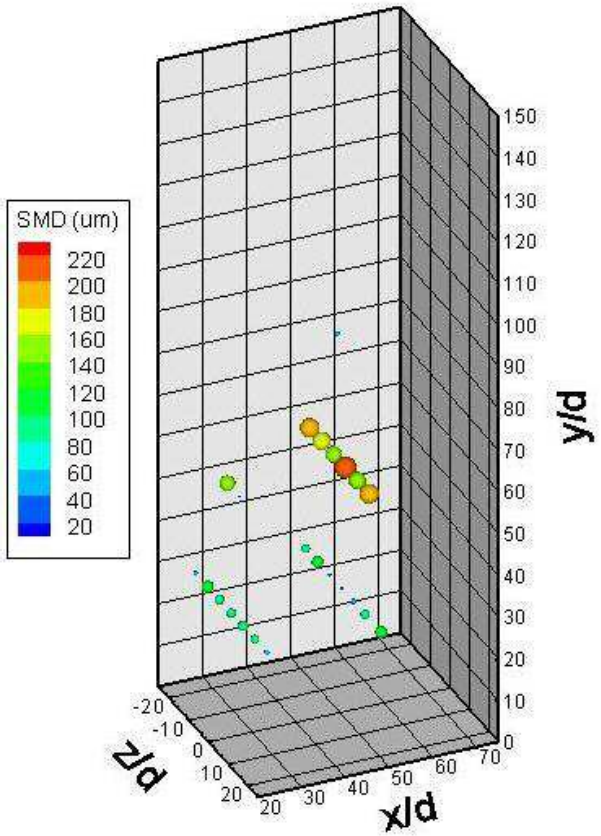

Figure A-4-19 SMD Distribution at GLR=4%, q_0=0.74, and d_0=0.5 mm

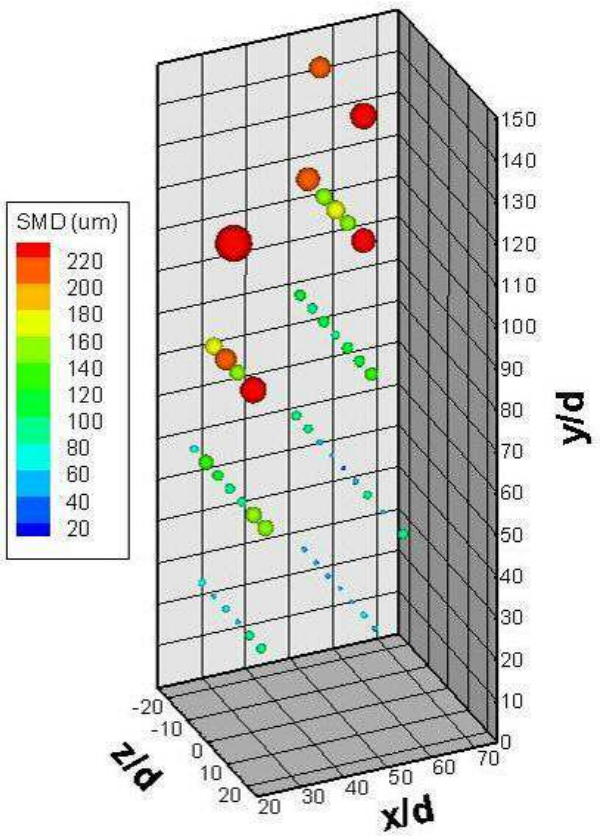

Figure A-4-20 SMD Distribution at GLR=4%, q_0=4, and d_0=0.5 mm

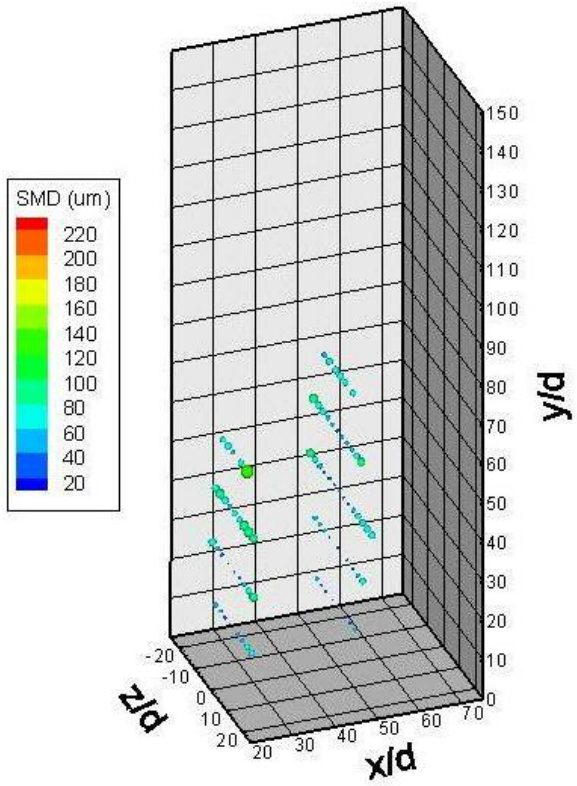

Figure A-4-21 SMD Distribution at GLR=8%, q_0=0.74, and d_0=1 mm

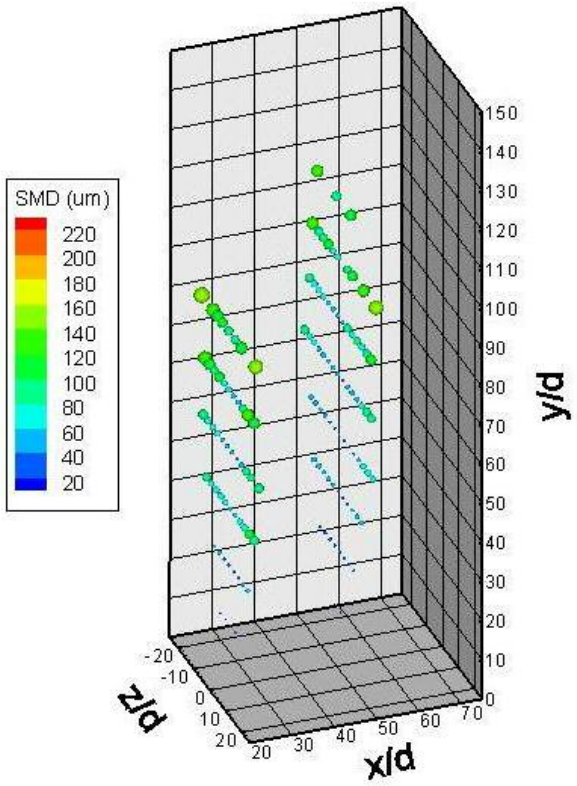

Figure A-4-22 SMD Distribution at GLR=8%, q_0=4, and d_0=1 mm

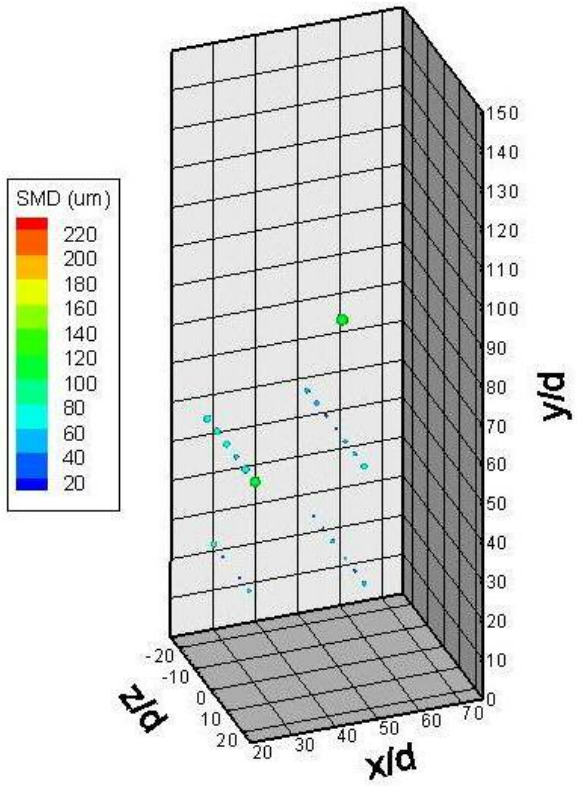

Figure A-4-23 SMD Distribution at GLR=8%, q_0=0.74, and d_0=0.5 mm

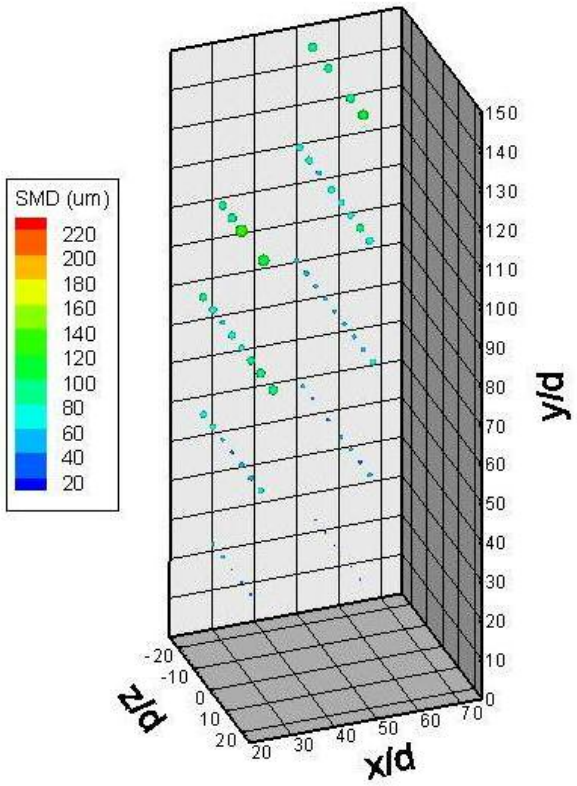

Figure A-4-24 SMD Distribution at GLR=8%, q_0=4, and d_0=0.5 mm

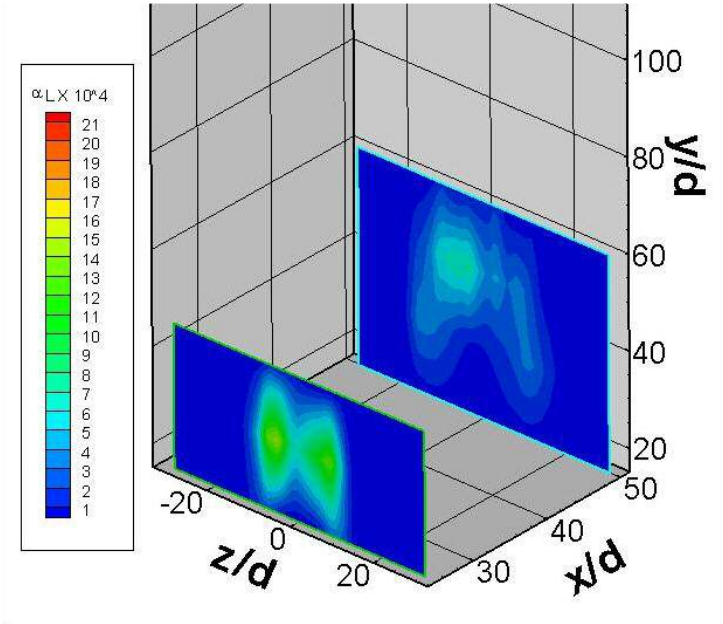

Figure A-4-25 Volume fraction plot at GLR=4%, q_0=0.74, and d_0=1 mm

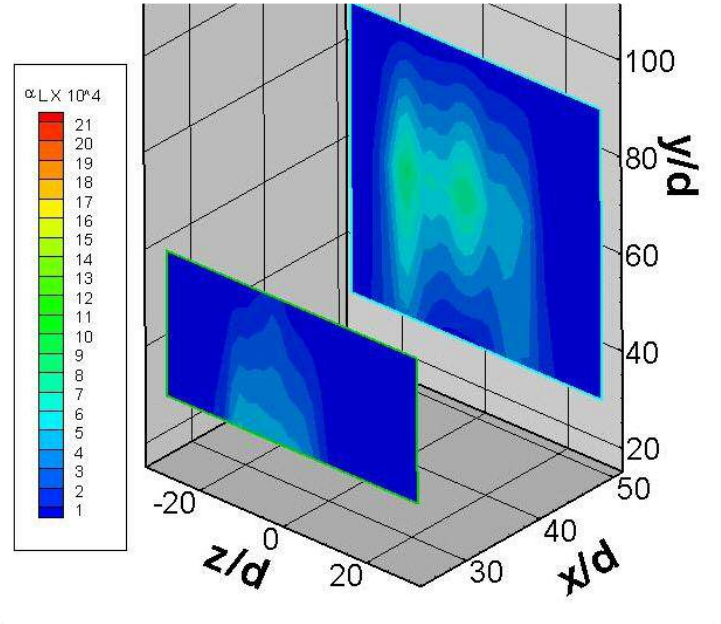

Figure A-4-26 Volume fraction plot at GLR=4%, q_0=0.74, and d_0=0.5 mm

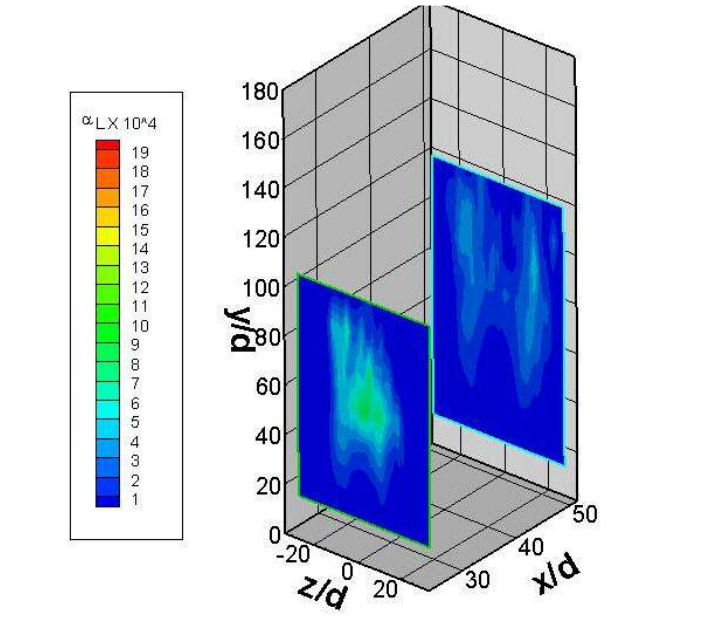

Figure A-4-27 Volume fraction plot at GLR=4%, q_0=4, and d_0=1 mm

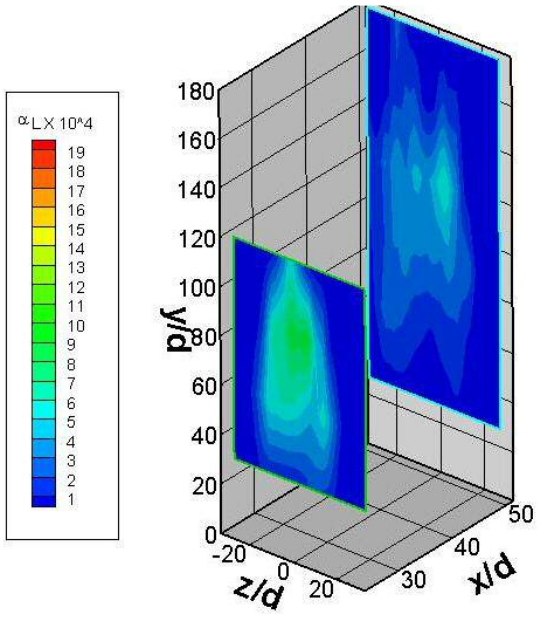

Figure A-4-28 Volume fraction plot at GLR=4%, q_0=4, and d_0=0.5 mm

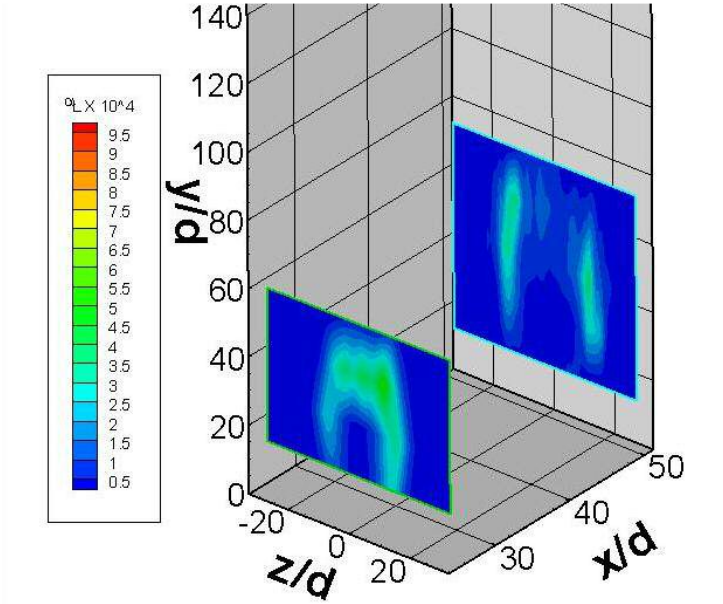

Figure A-4-29 Volume fraction plot at GLR=8%, q_0=0.74, and d_0=1 mm

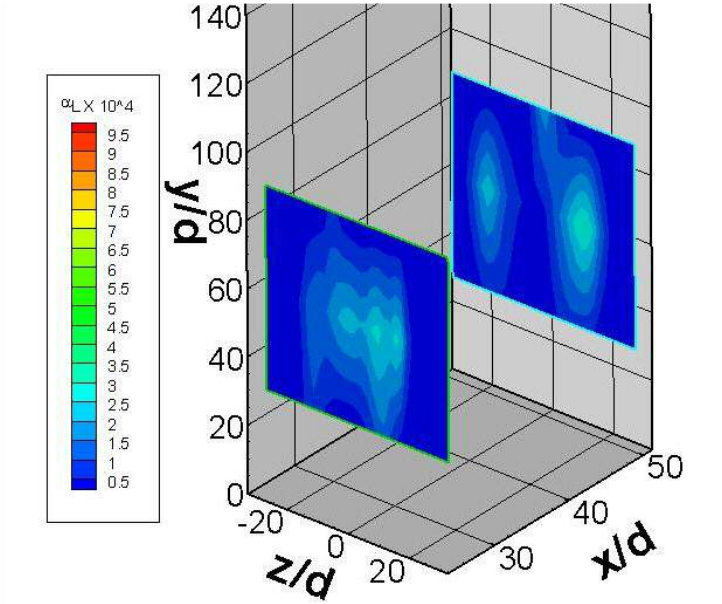

Figure A-4-30 Volume fraction plot at GLR=8%, q_0=0.74, and d_0=0.5 mm

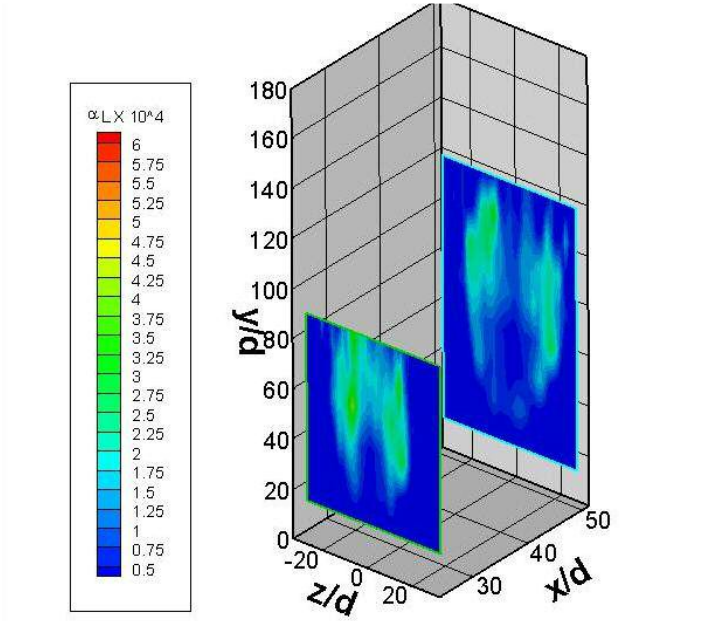

Figure A-4-31 Volume fraction plot at GLR=8%, q_0=4, and d_0=1 mm

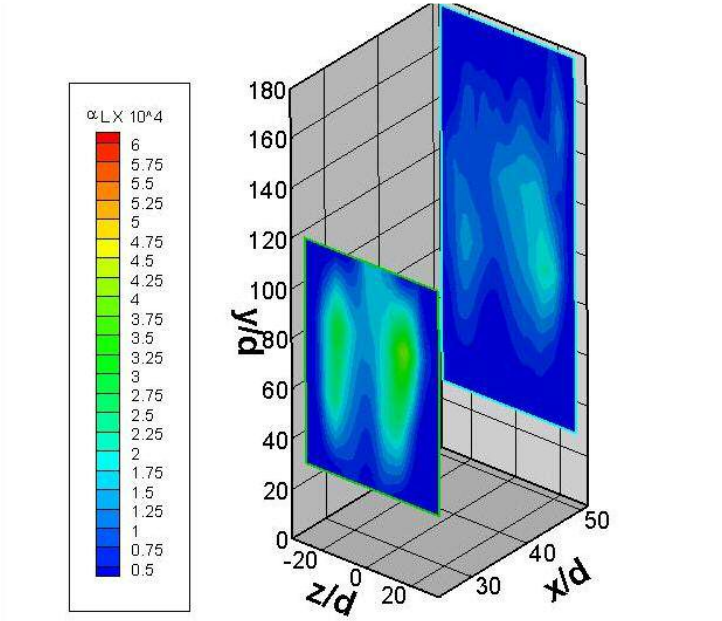

Figure A-4-32 Volume fraction plot at GLR=8%, q_0=4, and d_0=0.5 mm

Appendix B

Experimental Data

x/d	y/d	z/d	SMD (μm)
25	15	-11	86.56057
25	15	-8	61.45187
25	15	-5	58.76457
25	15	-1	22.14757
25	15	3	25.50889
25	15	6	45.95645
25	15	9	71.69292
25	30	-11	116.0985
25	30	-8	222.7592
25	30	-5	164.8767
25	30	-2	156.898
25	30	1	99.99748
25	30	4	116.8097
25	30	7	141.511
25	30	10	223.5618
25	45	-4	156.0832
25	45	7	143.9287
50	15	-14	51.77639
50	15	-11	43.63411
50	15	-8	34.87898
50	15	4	32.94537
50	15	7	49.86114
50	15	10	41.38593
50	15	14	70.3719
50	30	-15	116.4485
50	30	-12	88.71513
50	30	-9	61.43106
50	30	-6	50.19842
50	30	-3	31.29708
50	30	0	29.0164
50	30	3	34.31661
50	30	6	44.54453
50	30	9	59.61245
50	30	12	82.59887
50	30	15	86.75611

Table B-1 Data from the condition of 4% GLR, q_0=0.74, d_0=1 mm (SMD values averaged over 3 mm)

x/d	y/d	z/d	SMD (μm)
50	45	-15	151.0751
50	45	-12	117.5337
50	45	-9	144.1197
50	45	-6	132.8698
50	45	-3	182.1534
50	45	0	110.8062
50	45	3	101.5929
50	45	6	84.93296
50	45	9	115.7993
50	45	12	133.1803
50	45	18	134.0867
50	60	-4	166.368
50	60	0	81.00739

Table B-1 Continued…Data from the condition of 4% GLR, q_0=0.74, d_0=1 mm (SMD values averaged over 3

x/d	y/d	z/d	SMD (μm)
25	15	-11	54.24088
25	15	-8	42.02438
25	15	-5	39.40728
25	15	-2	19.04095
25	15	3	40.23117
25	15	6	44.99939
25	15	9	64.34183
25	15	12	65.90616
25	30	-13	79.17991
25	30	-10	53.12657
25	30	-7	36.92489
25	30	-3	21.08505
25	30	1	23.52154
25	30	4	34.40402

Table B-2 Data from the condition of 8% GLR, q_0=0.74, d_0=1 mm (SMD values averaged over 3 mm)

x/d	y/d	z/d	SMD (μm)
25	30	7	49.32101
25	30	10	66.94368
25	30	13	88.15518
25	45	-11	77.40752
25	45	-8	93.04268
25	45	-5	75.19045
25	45	-2	51.62819
25	45	1	61.94616
25	45	4	60.77807
25	45	7	96.58538
25	45	10	98.61097
25	45	13	89.31437
25	60	-6	63.02085
25	60	-3	74.5974
25	60	0	48.18304
25	60	5	68.34603
25	60	9	130.465
50	15	-14	43.15251
50	15	-11	29.79834
50	15	-8	30.14462
50	15	-4	25.28385
50	15	0	21.44067
50	15	4	27.26883
50	15	7	29.57563
50	15	10	44.16606
50	30	-15	54.38582
50	30	-12	42.85791
50	30	-9	40.90602
50	30	-6	27.52822
50	30	-1	31.00365
50	30	5	28.91867
50	30	9	28.75756
50	30	12	47.49109
50	30	15	66.81997
50	45	-18	88.02448
50	45	-15	63.442

Table B-2 Continued…Data from the condition of 8% GLR, q_0=0.74, d_0=1 mm (SMD values averaged over 3

x/d	y/d	z/d	SMD (μm)
50	45	-12	54.8329
50	45	-9	35.63872
50	45	-6	36.12292
50	45	-3	31.53988
50	45	0	26.56392
50	45	3	27.02914
50	45	6	35.56407
50	45	9	49.5716
50	45	12	62.92094
50	45	15	68.26044
50	45	18	72.4675
50	45	21	75.86037
50	60	-16	95.11979
50	60	-13	73.79255
50	60	-10	69.76236
50	60	-7	53.82982
50	60	-4	44.65487
50	60	-1	39.62269
50	60	2	42.34244
50	60	5	47.33256
50	60	8	49.76824
50	60	11	66.92005
50	60	14	86.79124
50	75	-9	58.15017
50	75	-6	68.74283
50	75	-2	75.14539
50	75	1	75.68067
50	75	4	66.23655
50	75	9	64.44396

Table B-2 Continued…Data from the condition of 8% GLR, q_0=0.74, d_0=1 mm (SMD values averaged over 3

x/d	y/d	z/d	SMD (μm)
25	15	-9	37.09835
25	15	-6	41.99386
25	15	-3	26.72621
25	15	2	24.22404
25	15	5	29.34274
25	15	8	33.26225
25	30	-14	66.3364
25	30	-11	55.80631
25	30	-8	58.76113
25	30	-5	22.4077
25	30	-2	18.88313
25	30	1	27.53188
25	30	4	33.58801
25	30	7	44.87349
25	30	10	61.36558
25	30	13	57.17282
25	45	-14	134.6384
25	45	-11	119.8442
25	45	-8	75.01111
25	45	-5	50.56789
25	45	-2	74.0109
25	45	1	42.68381
25	45	4	101.601
25	45	7	114.5202
25	45	10	89.84066
25	45	14	83.22126
25	60	-14	97.01278
25	60	-11	136.8722
25	60	-8	110.8121
25	60	-5	110.823
25	60	-2	97.97999
25	60	1	140.2997
25	60	4	130.7816
25	60	7	150.2999
25	60	10	149.9568

Table B-3 Data from the condition of 4% GLR, q_0=4, d_0=1 mm (SMD values averaged over 3 mm)

x/d	y/d	z/d	SMD (μm)
25	60	13	144.6189
25	75	-14	187.9408
25	75	-10	236.5428
25	75	-7	78.25676
25	75	-4	167.3395
25	75	-1	136.6838
25	75	3	251.2771
25	75	6	195.4629
25	75	10	196.6973
25	90	-13	280.8463
25	90	-9	261.1666
25	90	-3	204.8866
25	90	3	224.4557
50	15	-5	24.4127
50	15	6	19.76734
50	30	-15	44.78105
50	30	-12	44.6395
50	30	-9	36.89316
50	30	-6	19.45215
50	30	-3	27.14662
50	30	0	39.21553
50	30	3	35.70429
50	30	6	38.02731
50	30	9	45.22516
50	30	12	40.04899
50	30	15	42.67085
50	45	-17	63.93131
50	45	-14	60.30458
50	45	-11	46.15265
50	45	-8	32.58743
50	45	-5	25.32822
50	45	-2	22.96688
50	45	1	30.06029
50	45	4	30.74392
50	45	7	35.45854

Table B-3 Continued…Data from the condition of 4% GLR, q_0=4, d_0=1 mm (SMD values averaged over 3

x/d	y/d	z/d	SMD (μm)
50	45	10	50.68894
50	45	13	50.386
50	45	16	53.62624
50	45	19	72.18996
50	60	-19	70.7488
50	60	-16	68.13932
50	60	-13	52.19727
50	60	-10	45.54027
50	60	-7	33.71239
50	60	-4	31.04368
50	60	-1	36.7463
50	60	2	27.85648
50	60	5	36.20701
50	60	8	38.04215
50	60	11	57.36096
50	60	14	59.33277
50	60	17	63.86877
50	60	20	69.20123
50	60	24	95.31905
50	75	-21	95.60797
50	75	-17	77.61934
50	75	-14	71.95177
50	75	-11	72.25077
50	75	-8	64.62263
50	75	-5	52.275
50	75	-2	52.0548
50	75	1	48.56678
50	75	4	65.02123
50	75	7	64.89792
50	75	10	68.09671
50	75	13	77.11202
50	75	16	100.6565
50	75	19	119.036
50	90	-18	159.6059
50	90	-15	122.0744

Table B-3 Continued…Data from the condition of 4% GLR, q_0=4, d_0=1 mm (SMD values averaged over 3

x/d	y/d	z/d	SMD (μm)
50	90	-11	102.9297
50	90	-8	86.04571
50	90	-5	88.32948
50	90	-1	94.23025
50	90	4	65.87161
50	90	8	69.33588
50	90	11	111.1756
50	90	15	139.5343
50	90	21	164.5315
50	105	-22	173.4403
50	105	-15	156.6457
50	105	-12	139.5451
50	105	-8	138.1019
50	105	-3	124.601
50	105	3	121.2874
50	105	11	144.807
50	105	16	192.3896
50	105	25	208.7437
50	120	-11	187.4913
50	120	-8	134.257
50	120	3	137.287
50	120	13	207.449

Table B-3 Continued…Data from the condition of 4% GLR, q_0=4, d_0=1 mm (SMD values averaged over 3

x/d	y/d	z/d	SMD (μm)
25	15	-7	22.33321
25	15	-4	19.02555
25	15	-1	23.03071
25	15	2	27.98638
25	30	-11	43.83832
25	30	-8	50.09974
25	30	-5	35.28793
25	30	-2	35.93679
25	30	1	31.99786
25	30	4	36.5495
25	30	7	43.73681
25	30	10	48.61862
25	45	-16	88.6612
25	45	-13	61.13642
25	45	-10	71.35991
25	45	-7	71.15923
25	45	-4	61.10567
25	45	-1	42.11298
25	45	2	47.48275
25	45	5	63.61921
25	45	8	75.80623
25	45	11	100.8385
25	45	14	98.91245
25	60	-18	98.70062
25	60	-15	74.07068
25	60	-12	65.8958
25	60	-9	69.34329
25	60	-6	45.01869
25	60	-3	44.23103
25	60	0	45.30974
25	60	3	36.45195
25	60	6	59.71022
25	60	9	82.45979
25	60	12	82.56408
25	60	17	95.90175

Table B-4 Data from the condition of 8% GLR, q_0=4, d_0=1 mm (SMD values averaged over 3 mm)

x/d	y/d	z/d	SMD (μm)
25	75	-17	135.4789
25	75	-14	118.1113
25	75	-11	84.86788
25	75	-8	103.9877
25	75	-5	65.73215
25	75	-2	65.01783
25	75	1	56.3047
25	75	4	58.07286
25	75	7	81.89909
25	75	10	121.4479
25	75	14	116.6297
25	90	-19	156.1656
25	90	-12	134.4181
25	90	-9	119.0168
25	90	-6	102.4012
25	90	-2	92.13178
25	90	2	90.78471
25	90	6	119.7201
25	90	15	144.8009
50	15	-2	17.81279
50	15	2	21.28588
50	30	-11	35.41375
50	30	-8	37.19177
50	30	-5	37.99591
50	30	-2	30.72162
50	30	1	34.04757
50	30	4	38.81212
50	30	7	39.0055
50	30	10	28.22888
50	45	-15	57.98214
50	45	-12	56.31349
50	45	-9	46.71147
50	45	-6	52.31891
50	45	-3	41.58286
50	45	0	22.1077

Table B-4 Continued…Data from the condition of 8% GLR, q_0=4, d_0=1 mm (SMD values averaged over 3

x/d	y/d	z/d	SMD (μm)
50	45	3	31.57129
50	45	6	29.11494
50	45	9	40.88666
50	45	12	52.64594
50	45	15	56.11128
50	60	-17	56.73929
50	60	-14	50.71146
50	60	-11	41.69946
50	60	-8	44.9757
50	60	-5	33.22619
50	60	-2	29.97363
50	60	1	23.56977
50	60	4	28.04808
50	60	7	31.25605
50	60	10	33.15215
50	60	13	47.52574
50	60	16	65.7849
50	60	19	71.92261
50	60	22	64.91745
50	75	-21	92.92964
50	75	-18	63.37205
50	75	-15	65.7953
50	75	-12	48.56583
50	75	-9	57.74625
50	75	-6	43.02182
50	75	-3	47.72709
50	75	0	43.52715
50	75	3	32.7331
50	75	6	47.47278
50	75	9	57.87614
50	75	12	57.54446
50	75	15	67.81053
50	75	18	90.56732
50	75	21	91.95106
50	90	-18	90.75045

Table B-4 Continued…Data from the condition of 8% GLR, q_0=4, d_0=1 mm (SMD values averaged over 3

x/d	y/d	z/d	SMD (μm)
50	90	-15	75.02598
50	90	-12	68.50365
50	90	-9	63.79679
50	90	-6	57.02643
50	90	-3	56.73324
50	90	0	50.41963
50	90	3	43.66649
50	90	6	87.45202
50	90	9	66.2973
50	90	12	82.88892
50	90	15	73.41019
50	90	18	89.90479
50	90	21	108.6559
50	105	-16	126.2563
50	105	-12	94.67415
50	105	-9	90.46851
50	105	-6	100.9014
50	105	-3	65.57432
50	105	0	69.26014
50	105	6	84.21357
50	105	9	110.1729
50	105	16	123.0356
50	105	24	142.8576
50	120	-13	124.6444
50	120	-1	99.46176
50	120	8	116.7735

Table B-4 Continued…Data from the condition of 8% GLR, q_0=4, d_0=1 mm (SMD values averaged over 3

x/d	y/d	z/d	SMD (μm)
25	30	-18	41.8458
25	30	-12	114.4566
25	30	-6	93.69147
25	30	0	86.4899
25	30	6	98.20718
25	30	12	83.89333
25	30	18	51.68097
25	60	-2	146.678
25	60	4	29.43706
50	30	-18	80.12227
50	30	-12	111.2306
50	30	-6	34.18001
50	30	0	32.52653
50	30	6	48.30049
50	30	12	87.94364
50	30	20	113.9856
50	60	-16	180.5363
50	60	-10	168.617
50	60	-4	153.8118
50	60	2	203.1635
50	60	8	158.5613
50	60	14	181.8658
50	90	-2	47.32553

Table B-5 Data from the condition of 4% GLR, q_0=0.74, d_0=0.5 mm (SMD values averaged over 3 mm)

x/d	y/d	z/d	SMD (μm)
25	30	-12	60.39195
25	30	-6	34.16736
25	30	4	28.75398
25	30	10	44.5905
25	60	-16	76.73556
25	60	-10	70.94641
25	60	-4	71.55324
25	60	2	59.01833
25	60	8	76.72247
25	60	14	106.4001
50	30	-16	38.44139
50	30	-10	32.34591
50	30	-4	45.25953
50	30	4	40.80854
50	30	10	36.43771
50	30	16	54.69695
50	60	-20	57.16546
50	60	-14	58.02102
50	60	-8	39.97534
50	60	-2	33.01926
50	60	4	48.62881
50	60	10	45.96603
50	60	16	64.61721
50	90	2	119.7697

Table B-6 Data from the condition of 8% GLR, q_0=0.74, d_0=0.5 mm (SMD values averaged over 3 mm)

x/d	y/d	z/d	SMD (μm)
25	30	-14	73.96826
25	30	-8	53.87675
25	30	-2	62.31336
25	30	4	52.84241
25	30	10	87.73147
25	30	16	92.81051
25	60	-18	75.75904
25	60	-12	138.4493
25	60	-6	103.1743
25	60	0	95.16845
25	60	6	88.09527
25	60	12	153.3534
25	60	18	155.0895
25	90	-8	163.6704
25	90	-2	200.6918
25	90	4	147.0848
25	90	12	243.4752
25	120	2	339.5678
50	30	-18	52.23748
50	30	-12	47.08151
50	30	-6	49.02223
50	30	0	40.71904
50	30	6	45.77264
50	30	12	66.2239
50	30	18	55.31791
50	60	-22	91.9053
50	60	-16	85.04417
50	60	-10	58.69762
50	60	-4	45.28853
50	60	2	39.61841
50	60	8	59.84675
50	60	14	81.99071
50	60	22	47.25377
50	60	32	95.26371
50	90	-20	104.8765

Table B-7 Data from the condition of 8% GLR, q_0=0.74, d_0=0.5 mm (SMD values averaged over 3 mm)

x/d	y/d	z/d	SMD (μm)
50	90	-14	98.63909
50	90	-8	109.2889
50	90	-2	82.86272
50	90	4	109.179
50	90	10	106.9338
50	90	16	123.5386
50	120	-16	218.6498
50	120	-8	157.0641
50	120	-2	172.81
50	120	4	149.9289
50	120	12	224.6945
50	150	-10	200.3519
50	150	12	244.3992

Table B-7 Continued…Data from the condition of 8% GLR, q_0=0.744, d_0=0.5 mm (SMD values averaged

x/d	y/d	z/d	SMD (μm)
25	30	-12	42.45849
25	30	-6	43.14272
25	30	0	21.21701
25	30	6	37.84901
25	30	12	33.12665
25	60	-18	69.26786
25	60	-12	62.87532
25	60	-6	40.20693
25	60	0	38.05138
25	60	6	57.07765
25	60	12	58.07303
25	60	18	60.62581
25	90	-18	80.2048

Table B-8 Data from the condition of 8% GLR, q_0=4, d_0=0.5 mm (SMD values averaged over 3 mm)

x/d	y/d	z/d	SMD (μm)
25	90	-12	77.13095
25	90	-6	53.72844
25	90	0	75.32751
25	90	6	61.54948
25	90	12	80.76542
25	90	18	90.4375
25	90	26	96.08324
25	120	-6	82.86864
25	120	0	91.57309
25	120	6	122.3684
25	120	20	115.6414
50	30	-14	23.15852
50	30	-8	20.79614
50	30	-2	21.80564
50	30	8	17.7133
50	30	14	21.1697
50	60	-22	43.55117
50	60	-16	35.96281
50	60	-6	36.47746
50	60	2	40.97044
50	60	8	42.06129
50	60	14	39.69758
50	60	20	50.62944
50	90	-26	51.9199
50	90	-20	56.44144
50	90	-14	46.83331
50	90	-8	43.79461
50	90	-2	40.02795
50	90	4	48.25993
50	90	10	47.01185
50	90	16	53.56066
50	90	22	66.27529
50	120	-24	76.92781
50	120	-18	76.097
50	120	-12	57.02554

Table B-8 Continued…Data from the condition of 8% GLR, q_0=4, d_0=0.5 mm (SMD values averaged over 3

x/d	y/d	z/d	SMD (μm)
50	120	-4	76.6527
50	120	2	67.88333
50	120	8	68.78041
50	120	14	80.68165
50	120	20	79.95192
50	150	-16	95.55546
50	150	-6	88.76581
50	150	8	94.23023
50	150	16	102.6983

Table B-8 Continued…Data from the condition of 8% GLR, q_0=4, d_0=0.5 mm (SMD values averaged over 3

VITA

Brian Derrick Miller

Candidate for the Degree of

Master of Science

Thesis: BREAKUP OF AERATED-LIQUID JETS IN A SUBSONIC CROSSFLOW

Major Field: Mechanical Engineering

Biographical:

Personal Data: Born in Oklahoma, May 15, 1982, the son of Brent Miller and Tonya Parker

Education: Received Bachelor of Science degree in Mechanical Engineering from Oklahoma Christian University, Edmond, Oklahoma in December 2004. Completed the requirements for Master of Science degree in Mechanical Engineering from Oklahoma State University, Stillwater, Oklahoma in December 2006.

Experience: Employed by Oklahoma State University as a teaching assistant for Engineering Design with CAD, Compressible Flow, and Experimental Fluid Dynamics from January 2005 to May 2006. Employed by Oklahoma State University as a machine shop supervisor from June 2005 to December 2006.

Professional Memberships: The American Society of Mechanical Engineering.

Name: Brian Derrick Miller Date of Degree: December, 2006

Institution: Oklahoma State University Location: Stillwater, Oklahoma

Title of Study: DIGITAL HOLOGRAPHIC DIAGNOSITCS OF AERATED-LIQUID JETS IN A SUBSONIC CROSSFLOW

Pages in Study: 92 Candidate for the Degree of Master of Science

Major Field: Mechanical Engineering

Scope and Method of Study: Different methods of digital holography were investigated to determine their ability to measure the properties of a spray produced by an aerated-liquid jet. The chosen method was then used to observe the properties of the spray at different downstream locations. Different test conditions of: 1 mm and 0.5 mm injector exit diameters, 4% and 8% GLR, 25 and 50 jet diameters downstream, and jet-to-freestream momentum ratios of 0.74 and 4, were observed to determine their effects. The observations were made by producing maps of the Sauter mean diameter distribution throughout the spray, as well as volume fraction plots showing the concentration of the droplets within the spray.

Findings and Conclusions: An aerated jet in crossflow was studied and it was found that digital holographic microscopy was the best method for resolving the smallest droplets within the spray. Using this technique Sauter mean diameter maps were produced and the different effects could be investigated. It was found that the gas-to-liquid mass flow rate ratio had the most effect on droplet sizes, and the SMD could be normalized by this film thickness to produce comparable SMD sizes across different test conditions. This was in contrast to the effect of jet diameter which had little effect on the spray. It was also found that the jet-to-freestream momentum ratio strongly affected the penetration height of the spray into the crossflow while having a small effect on the droplet sizes. Evidence of secondary breakup was also found between the two downstream locations. This evidence was the reduction in droplet sizes, and a study of the aerodynamic forces on the droplets in this area. It was found that at the 4% GLR conditions secondary breakup is likely occurring due to the larger droplets produced at this condition.

ADVISER'S APPROVAL: Khaled A. Sallam